ASME Journal of Dynamic Systems, Measurement, and Control
Online journal at:
https://asmedigitalcollection.asme.org/dynamicsystems

Exergy Management Strategies for Hybrid Electric Ground Vehicles: A Dynamic Programming Solution

Matteo Acquarone[1]
Department of Energy (DENERG),
Politecnico di Torino,
Torino 10129, Italy
e-mail: matteo.acquarone@polito.it

Gabriele Pozzato
Energy Science and Engineering,
Stanford University,
Stanford, CA 94305
e-mail: gpozzato@stanford.edu

Corey James
Department of Chemistry and Life Science,
United States Military Academy,
West Point, NY 10996
e-mail: corey.james@westpoint.edu

Simona Onori
Energy Science and Engineering,
Stanford University,
Stanford, CA 94305
e-mail: sonori@stanford.edu

In this work, exergy management strategies (ExMSs) for hybrid electric ground vehicles (HEVs) are developed. The main advantage of using the exergetic framework is the possibility of pursuing unconventional optimization goals that are inaccessible to the standard energy management strategy (EMS). For instance, in military applications, the critical goal of preventing thermal imaging detection from adversary units does not seem achievable with the conventional EMS. On the other hand, the exergy-based framework can be adopted to reduce the vehicle thermal emissions through the minimization of exergy terms related to heat exchange. Moreover, the overall efficiency of the vehicle can be increased through the minimization of the exergy destruction, a quantity that is not quantifiable by energy-based methods. In this paper, the exergetic model of a series hybrid electric military truck and the exergetic model of the electric induction generator are developed and used to formulate and solve two novel exergy management strategies aiming to minimize genset exergy destruction and thermal emissions, respectively. The optimal solutions to the EMS and ExMSs control problems are obtained through Dynamic Programming over two driving missions. The results show that ExMS for the minimization of exergy destruction achieves similar results to the standard EMS, while the ExMS for the minimization of thermal emissions obtains significantly lower thermal emissions compared to the EMS, effectively reducing the thermal imaging detection risk. [DOI: 10.1115/1.4063610]

1 Introduction

Battery electric vehicles represent the most appealing solution for clean transportation for civil applications due to their zero tank-to-wheel emissions and high efficiency technology. However, for military applications, full electrification of the powertrain is not a practical solution mainly due to the logistical challenges related to vehicle charging on the battlefield. Since recharging stations are not available on the battlefield, once the energy storage is depleted, the vehicle crew would be exposed while waiting for the assistance of another vehicle to recharge the battery [1]. Other significant hurdles to full electrification of tactical military vehicles are the relatively high weight and volume of the battery pack and the limited range. For instance, electrifying an M1Abrams tank would require a greater than 10 fold increase in power source weight and volume,[2] with other vehicles showing similar increases [2]. These substantial increases are further reasons that full electrification is currently impractical. In this context, HEVs are the best solution to achieve improved vehicle performance while reducing emissions and saving fuel [3].

Power-split strategies in HEVs are generally designed using energy-based methodologies [4] focusing on fuel consumption (FC) minimization. The energetic analysis is useful to study energy conversion during a process, but it is not meant to quantify the irreversibilities that result from it. On the other hand, the exergetic analysis can provide understanding of a process by assessing the sources of inefficiency associated with it [5]. Exergy is defined as the maximum useful work that can be obtained from a thermodynamic system or process with respect to a given reference state [6]. Based on the first and second laws of thermodynamics, exergy analysis provides the magnitude, locations, and causes of the irreversibilities of a process and is used to measure the quality of energy transfer.

Exergy analysis has been used in a variety of applications, such as modeling and design optimization of power plants [7], photovoltaic systems [8], and aerospace technologies [9,10]. Common exergetic optimization goals are the minimization of exergy destruction and exergy losses, two quantities that lead to the reduction of the available exergy of a system. Exergy destruction accounts for all the irreversibilities of a process, which are quantified by the entropy generation through the second law of thermodynamics. On the other hand, the exergy losses account for all the exergy transfer terms due to heat, mass, or work leaving the system. An example of exergy destruction minimization is found in Ref. [11], where the temperature and pressure in several points of a nuclear-solar power

[1]Visiting Scholar at the Department of Energy Science and Engineering, Stanford University.

[2]The weight and volume of a battery containing the same amount of energy of a M1Abrams fuel tank would be around 30,342 kg and 11.6 m^3. These estimates are obtained assuming a fuel tank volume of 1.89 m^3, a fuel energy density of 10,435 kWh/m^3, a fuel conversion efficiency of 40%, a battery energy density of 260 Wh/kg, and a battery volumetric energy density 680 kWh/m^3.

Contributed by the Dynamic Systems Division of ASME for publication in the JOURNAL OF DYNAMIC SYSTEMS, MEASUREMENT, AND CONTROL. Manuscript received March 23, 2023; final manuscript received September 14, 2023; published online January 11, 2024. Assoc. Editor: Mahdi Shahbahkti.

plant are optimally selected to minimize the exergy destruction of the whole power plant system. The improved power plant operates more effectively in producing energy and fresh water.

Exergy analysis has also been utilized in the development of various systems' control strategies [12]. In Ref. [13], model predictive control (MPC) is applied to minimize the exergy destruction of a heating, ventilation, and air conditioning system. The exergy-based MPC outperforms the energy-based MPC and rule-based algorithm by achieving lower exergy destruction and energy consumption. Jain and Alleyne [14] developed an accurate exergetic model of a vapor compression system and designed an exergy-based controller to increase its efficiency. The novel MPC effectively rejects disturbances, such as weather and varying load, while achieving over 40% higher exergetic efficiency than a common energy-based MPC. In large capacity boiler control systems, a novel control technique is introduced in Ref. [15] to maintain the steam temperatures of a superheater close to the design specifications by means of spray flows. The solution shows that the exergy destruction rates vary significantly with changes in the distributions of spray flows. This conclusion could have not been drawn using simpler energy-based optimization techniques. Exergy-based control strategies have recently expanded in the naval sector [16,17] for lower waste emissions and fuel consumption, showing the possibility of using the exergetic approach to develop lighter, smaller, and more effective ship systems.

In the context of ground vehicles, exergy analysis and control have been widely used in internal combustion engines (ICEs) [18]. In Refs. [19] and [20], energy and exergy analyses are performed considering different fuel typologies. A crank-angle resolved ICE exergy model along with an optimal control algorithm based on exergy for transient and steady-state operation of ICE is presented in [21]. The proposed algorithm finds the optimum combustion phasing to maximize the second law of thermodynamics efficiency, reaching fuel savings higher than 5% with respect to the traditional energy-based combustion control. The first comprehensive vehicle exergy modeling framework for HEVs is found in Ref. [22]. Exergy transfer and destruction terms are quantified for each component of the powertrain and the whole vehicle exergetic balance is developed. The results obtained over the WLTC driving cycle show that the ICE contributes to about 80% of the exergy destruction and losses of the whole vehicle. In this paper, we focus on offline ExMSs to control the power split of HEVs. To the best of the authors' knowledge, this is the first time that exergetic modeling has been adopted in the context of optimization of HEVs operation. Exergy-based modeling and control methods provide multiple advantages compared to conventional HEV energy management methods. First, the exergy-based control strategies enable the pursuit of nonstandard optimization goals that are not feasible with the conventional energy management, such as the minimization of exergy destruction. In the context of military vehicles applications, the reduction of thermal imaging detection risk is a critical goal [23] that cannot be achieved by the conventional EMS. The exergetic framework is used in this work to reduce thermal emissions by minimizing exergy transfer due to heat exchange. Another key advantage of the exergy-based over the energy-based approach is that exergy modeling allows to combine terms of different nature into one balance equation. For instance, exergy destruction can be directly summed up to exergy transfer due to mass transport or heat exchange. This allows the formulation of optimization problems to minimize different exergetic terms without the need to change the modeling framework. Two novel ExMSs are formulated to minimize genset exergy destruction and thermal emissions, respectively, and the optimal solutions are obtained through the Dynamic Programming algorithm. The HEV exergetic modeling is built upon our previous work in Ref. [22]. The vehicle exergetic model is enhanced by including the detailed ICE exergy model developed in Ref. [24] and used in Ref. [25]. Moreover, in this paper, a new exergy model for induction machines (IM), that transcends HEV applications and can be applied in battery electric vehicles, is developed. This work lays the foundation for the development of online management strategies and design optimization algorithms for ground vehicles.

The remainder of the paper is organized as follows: In Sec. 2, the military HEV powertrain model and its components are recalled and the new genset exergetic model is formulated. Section 3 presents the optimal control problems (OCPs) for the standard EMS and novel ExMSs. In Sec. 4, results obtained through Dynamic Programming for the ExMSs are analyzed and compared with the standard EMS. Finally, conclusions are discussed in Sec. 5.

2 Vehicle Model

In this section, the model of a series hybrid electric mine-resistant ambush-protected all-terrain vehicle (M-ATV) is recalled from Refs. [26] and [27]. The powertrain configuration is schematically shown in Fig. 1. Its main components include a 260 kW ICE, a 268 kW electric Induction generator, a 10.9 kWh lithium-ion battery pack, and four 95 kW Interior Permanent Magnet Synchronous in-hub Motors (IPMSM). The battery pack is connected to the generator and traction motors through the AC–DC and AC–AC converters [28]. The vehicle model is developed following a backward-facing paradigm where the target speed, provided as input to the model in the form of a driving cycle, is perfectly tracked by the vehicle. The resulting power required at the wheels is computed and propagated back to the power sources, ICE and battery pack, through the drivetrain [4]. The gearbox (GB) efficiency is assumed to be unitary. The symbols and units of the parameters used in the models of the vehicle and powertrain components are specified in the nomenclature table. The ICE and the generator are lumped together into the genset [29]. The exergetic model of the genset system is derived in this section starting from Refs. [22] and [24].

2.1 Reference State. Exergy is defined as the maximum amount of work that can be produced by a flow of matter or energy as it comes to equilibrium with a reference state [30]. In this work, the reference state is characterized by the environment pressure $P_0 = 1\text{bar}$ and temperature $T_0 = 25\,^\circ\text{C}$.

2.2 Longitudinal Vehicle Dynamics. The power requested at the wheels P_w is computed from the longitudinal vehicle dynamics equation: $P_w = v(M\dot{v} + F_{\text{brake}} + Mg\sin\theta + C_r Mg\cos\theta + \frac{1}{2}\rho_a A C_x v^2)$, where v is the vehicle velocity, M is the vehicle mass, F_{brake} is the mechanical brake force, C_r and C_x are the roll and drag coefficients, respectively, ρ_a is the air density, A is the frontal area of the vehicle, and θ is the road slope [4].

2.3 Electric Traction Motors. The traction power requested at the wheels is propagated backward to the four electric motors. The electric power required by a single electric motor $P_{\text{mot},e}$ satisfies the following balance equation:

$$4P_{\text{mot},e} + P_{\text{aux}} = P_{\text{gen}} + P_{\text{batt}} \tag{1}$$

where P_{gen} and P_{batt} are the generator and battery power, respectively, and P_{aux} is the power required by the auxiliary systems onboard. This relation is true under the assumption that the efficiency of the AC–DC and AC–AC converters is unitary. Each motor is an IPMSM characterized by static efficiency maps, which are functions of motor speed ω_{mot} and torque τ_{mot}. The relation between the electric $P_{\text{mot},e}$ and mechanical power $P_{\text{mot},m}$ of the electric motor is then expressed using the motor efficiency η_{mot}

$$P_{\text{mot},e} = \begin{cases} \dfrac{P_{\text{mot},m}}{\eta_{\text{mot}}}, & \text{if } P_{\text{mot},m} \geq 0 \\ P_{\text{mot},m} \cdot \eta_{\text{mot}}, & \text{if } P_{\text{mot},m} < 0 \end{cases} \tag{2}$$

The mechanical power $P_{\text{mot},m}$ is calculated from the gearbox efficiency η_{GB} and P_w through the following equation:

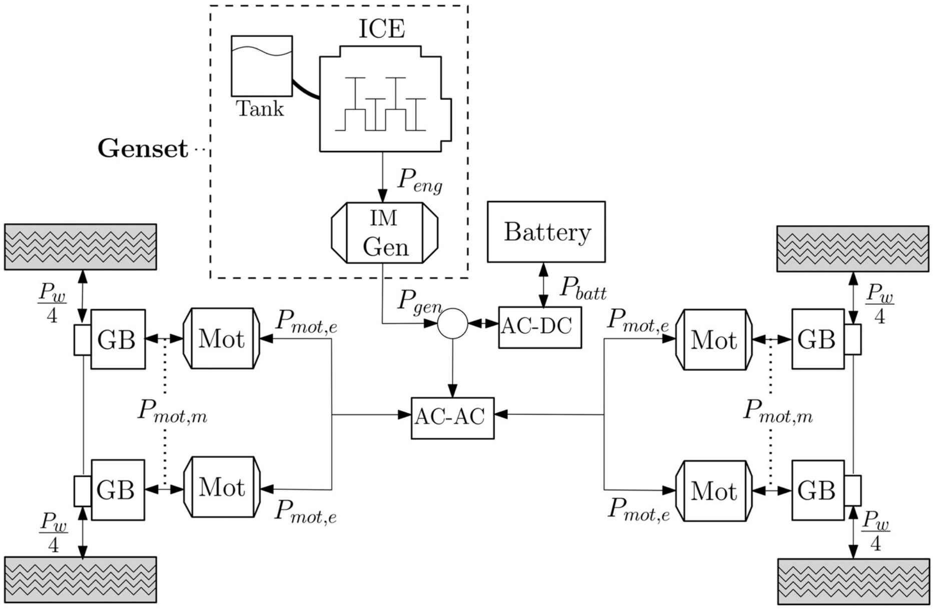

Fig. 1 Series HEV configuration

$$P_{\mathrm{mot},m} = \begin{cases} \dfrac{P_w}{4 \cdot \eta_{\mathrm{GB}}}, & \text{if } P_w \geq 0 \\ \dfrac{P_w \cdot \eta_{\mathrm{GB}}}{4}, & \text{if } P_w < 0 \end{cases} \tag{3}$$

where P_w, and $P_{\mathrm{mot},m}$ are considered positive during the traction phases, and negative during braking. To formulate the exergy model for the electric motor, power losses, and thermal dynamics formulations are borrowed from Ref. [22]. The motor losses are divided into copper losses $P_{\mathrm{SCL,mot}}$, iron losses $P_{\mathrm{iron,mot}}$ and friction losses $P_{\mathrm{fric,mot}}$. The temperature T_{mot} of the IPMSM is evaluated through the following thermal model, which accounts for power losses and heat exchange $\dot{Q}_{\mathrm{heat,mot}}$ between the motor and the environment:

$$\begin{aligned} C_{\mathrm{mot}} \cdot \dot{T}_{\mathrm{mot}} &= \dot{Q}_{\mathrm{heat,mot}} + P_{\mathrm{SCL,mot}} + P_{\mathrm{iron,mot}} + P_{\mathrm{fric,mot}} \\ \dot{Q}_{\mathrm{heat,mot}} &= h_{\mathrm{out,mot}}(T_0 - T_{\mathrm{mot}}) \end{aligned}$$

where $h_{\mathrm{out,mot}}$ is the convective heat transfer coefficient between the IPMSM and the environment. The exergy destruction $\dot{X}_{\mathrm{dest,mot}}$ and exergy transfer due to heat exchange with the surroundings $\dot{X}_{\mathrm{heat,mot}}$ are computed according to the following equations [22]:

$$\begin{aligned} \dot{X}_{\mathrm{heat,mot}} &= \left(1 - \frac{T_0}{T_{\mathrm{mot}}}\right) \cdot \dot{Q}_{\mathrm{heat,mot}} \\ \dot{X}_{\mathrm{dest,mot}} &= -\frac{T_0 \cdot (P_{\mathrm{SCL,mot}} + P_{\mathrm{iron,mot}} + P_{\mathrm{fric,mot}})}{T_{\mathrm{mot}}} \end{aligned} \tag{4}$$

2.4 Battery Model. The energy storage used in the vehicle is a 10.9 kWh lithium-ion battery pack comprising $N_S = 124$ and $N_P = 5$ Nickel Manganese Cobalt (NMC)/Graphite cells in series and parallel configuration, respectively. Each cell is modeled through a zero-order equivalent circuit model (ECM) [29]. The ECM parameters, internal resistance $R_{0,\mathrm{cell}}$ and open circuit voltage $\mathrm{OCV}_{\mathrm{cell}}$, are obtained from the experimental data in Refs. [31] and [32], respectively. $R_{0,\mathrm{cell}}$ is calculated from the 1C discharge pulse test at $T_{\mathrm{cell}} = 25\,^{\circ}\mathrm{C}$, and shown in Fig. 2; the $\mathrm{OCV}_{\mathrm{cell}}$ is obtained from the constant current discharge test at C/20 for three different temperatures, shown in Fig. 3, assuming that the measured battery terminal voltage is approximately equal to the open circuit voltage.

Cells are assumed to be electrically homogeneous and to behave all in the same way. Therefore, the cell-level electrical quantities can be upscaled to the pack level as follows: $R_{0,\mathrm{batt}} = \frac{N_S}{N_P} \cdot R_{0,\mathrm{cell}}$, $\mathrm{OCV}_{\mathrm{batt}} = N_S \cdot \mathrm{OCV}_{0,\mathrm{cell}}$, $Q_{\mathrm{batt}} = N_P \cdot Q_{\mathrm{cell}}$, where $R_{0,\mathrm{batt}}$, $\mathrm{OCV}_{\mathrm{batt}}$, and Q_{batt} are the battery pack internal resistance, open circuit voltage, and capacity, respectively. The state of charge of the battery (SOC) rate of the battery pack is calculated through the following equation:

$$\begin{aligned} \dot{\mathrm{SOC}}_{\mathrm{batt}} &= -\frac{I_{\mathrm{batt}}}{Q_{\mathrm{batt}}} \\ I_{\mathrm{batt}} &= \frac{\mathrm{OCV}_{\mathrm{batt}} - \sqrt{\mathrm{OCV}_{\mathrm{batt}}^2 - 4R_{0,\mathrm{batt}}P_{\mathrm{batt}}}}{2R_{0,\mathrm{batt}}} \end{aligned} \tag{5}$$

In the remainder of the paper, the symbol SOC is used to denote $\mathrm{SOC}_{\mathrm{batt}}$. The property of modularity in a battery pack guarantees that the thermal behavior of a cell does not change upon its interconnection with other cells [33]. Although thermal modularity of all the battery cells is, in general, not guaranteed [34], in this work, it is assumed considering that there is no heat exchange between the battery cells; hence, the thermal gradient across the cells is zero [35],

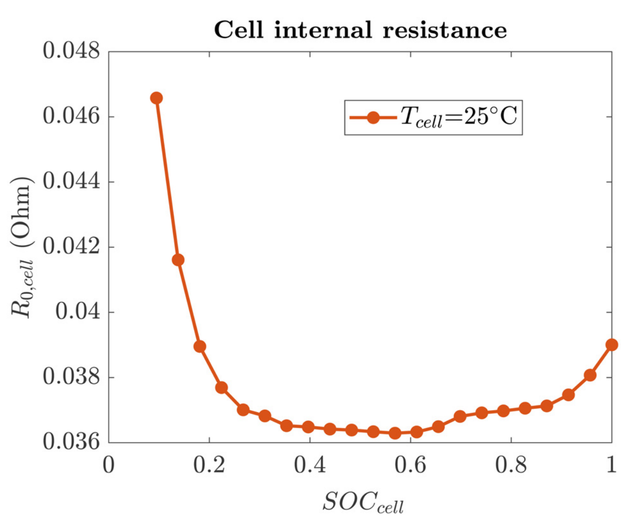

Fig. 2 Internal resistance as a function of the SOC for a NMC cell at temperature T_{cell} equal to 25 °C

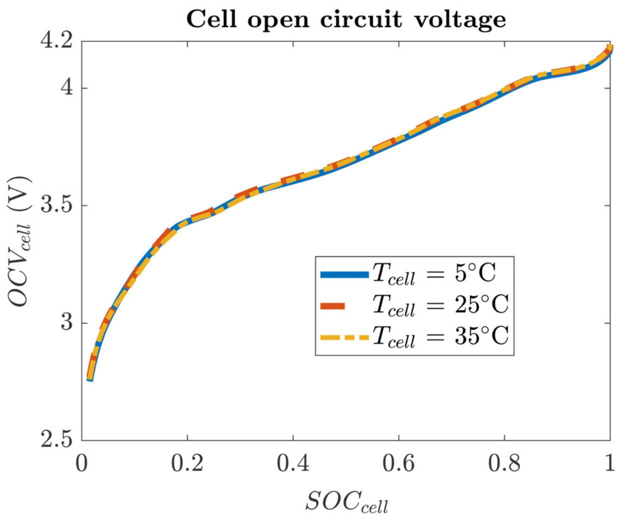

Fig. 3 Open circuit voltage as a function of the SOC for a NMC cell at temperatures T_{cell} equal to 5, 25, and 35 °C

and the battery pack temperature T_{batt} can be assumed equal to the cell temperature, $T_{\text{batt}}(t) = T_{\text{cell}}(t)$.

Under these assumptions, the battery pack temperature behavior represents a lower bound of the actual battery pack temperature one would obtain under real operation. To evaluate the battery cell temperature T_{cell}, the thermal cell model is introduced. A simple lumped model accounting for Joule losses and convective heat transfer $\dot{Q}_{\text{heat,cell}}$ between battery cell (T_{cell}) and surroundings (T_0) is used

$$\begin{aligned} C_{\text{cell}} \cdot \dot{T}_{\text{cell}} &= R_{0,\text{cell}} \cdot I_{\text{cell}}^2 + \dot{Q}_{\text{heat,cell}} \\ \dot{Q}_{\text{heat,cell}} &= h_{\text{out,cell}}(T_0 - T_{\text{cell}}) \end{aligned} \tag{6}$$

where C_{cell} and $h_{\text{out,cell}}$ are the thermal capacity and convective heat transfer coefficient of a cell, respectively. To compute the battery pack exergetic terms, the heat exchanged between the battery pack and the environment $\dot{Q}_{\text{heat,batt}}$, is obtained upscaling the cell-level convective heat transfer $\dot{Q}_{\text{heat,cell}}$ as $\dot{Q}_{\text{heat,batt}} = N_S \cdot N_P \cdot \dot{Q}_{\text{heat,cell}}$.

The exergy model of the battery pack is borrowed from Ref. [22]. The exergy destruction $\dot{X}_{\text{dest,batt}}$ and exergy transfer $\dot{X}_{\text{heat,batt}}$ due to the heat exchange of the battery pack are written as follows:

$$\begin{aligned} \dot{X}_{\text{heat,batt}} &= \left(1 - \frac{T_0}{T_{\text{batt}}}\right) \cdot \dot{Q}_{\text{heat,batt}} \\ \dot{X}_{\text{dest,batt}} &= -\frac{T_0}{T_{\text{batt}}} R_{0,\text{batt}} \cdot I_{\text{batt}}^2 \end{aligned} \tag{7}$$

It is worth noting that beyond the experiments needed to estimate the electrical and thermal parameters of the battery, no additional experiment is required to obtain the battery exergy terms. Indeed, the battery exergy destruction can be easily determined in real applications by knowing the battery internal resistance and measuring or computing the battery current and battery temperature. To compute the exergetic term $\dot{X}_{\text{heat,batt}}$, the cell-level thermal parameters are needed and battery temperature must be measured or estimated. Moreover, no battery exergy term is a function of the battery electrical capacity.

2.5 Electric Generator. Since the electric generator is not an IPMSM, the IPMSM exergetic model developed in Ref. [22] cannot be used for quantifying the generator exergetic terms. Therefore, a new exergetic model for Induction Machines is formulated.

First, the power losses of the IM are evaluated to calculate the exergetic terms related to exergy destruction and heat transfer. The power losses of an IM are divided into stator copper losses $P_{\text{SCL,IM}}$, rotor copper losses $P_{\text{RCL,IM}}$, iron losses $P_{\text{iron,IM}}$, and friction losses $P_{\text{fric,IM}}$. Losses that fall outside of the aforementioned categories are referred to as stray losses [36]. Since stray losses are usually less than 1% of the total power losses $P_{\text{loss,IM}}$, they can be neglected. Hence, the energetic balance of the IM is described by the following equation:

$$\begin{aligned} P_{\text{out,IM}} &= P_{\text{in,IM}} - P_{\text{loss,IM}} \\ P_{\text{loss,IM}} &= P_{\text{SCL,IM}} + P_{\text{RCL,IM}} + P_{\text{iron,IM}} + P_{\text{fric,IM}} \end{aligned} \tag{8}$$

where $P_{\text{out,IM}}$ and $P_{\text{in,IM}}$ are the useful output work and the input power of the IM, respectively. The energetic efficiency η_{IM} of the IM is written as follows:

$$\eta_{\text{IM}} = \frac{P_{\text{out,IM}}}{P_{\text{in,IM}}} \tag{9}$$

The IM power losses are derived using the IM equivalent circuit model, and are expressed as a function of speed ω_{IM}, torque τ_{IM}, and temperature T_{IM}; their formulation is fully detailed in Appendix A. To assess the evolution of T_{IM} over time, the thermal model of the IM is formulated considering the power losses and the heat transfer $\dot{Q}_{\text{heat,IM}}$ between the motor and the surroundings

$$\begin{aligned} C_{\text{IM}} \cdot \dot{T}_{\text{IM}} &= \dot{Q}_{\text{heat,IM}} + P_{\text{SCL,IM}} + P_{\text{RCL,IM}} + P_{\text{iron,IM}} + P_{\text{fric,IM}} \\ \dot{Q}_{\text{heat,IM}} &= h_{\text{out,IM}}(T_0 - T_{\text{IM}}) \end{aligned} \tag{10}$$

where C_{IM} and $h_{\text{out,IM}}$ are the IM thermal capacity and convective heat transfer coefficient, respectively.

The power losses can be used to calculate the exergetic terms of the IM. The modeled exergy terms of the IM are the exergy transfer $\dot{X}_{\text{heat,IM}}$ due to the heat exchange between the generator and the environment, the useful work $\dot{X}_{\text{work,IM}}$ produced by the IM, and the exergy destruction $\dot{X}_{\text{dest,IM}}$. Terms associated with exergy destruction and heat of the electric IM are calculated with the same formulation as [22]

$$\begin{aligned} \dot{X}_{\text{heat,IM}} &= \left(1 - \frac{T_0}{T_{\text{IM}}}\right) \cdot \dot{Q}_{\text{heat,IM}} \\ \dot{X}_{\text{work,IM}} &= -\omega_{\text{IM}} \cdot \tau_{\text{IM}} \\ \dot{X}_{\text{dest,IM}} &= -\frac{T_0 \cdot (P_{\text{SCL,IM}} + P_{\text{RCL,IM}} + P_{\text{iron,IM}} + P_{\text{fric,IM}})}{T_{\text{IM}}} \end{aligned} \tag{11}$$

If the IM equivalent circuit parameters and thermal parameters are known, each IM exergy term can be calculated for every triplet (ω_{IM}, τ_{IM}, T_{IM}). The main difference between the IM exergy model and IPMSM exergy model of [22] is related to the rotor copper power loss term $P_{\text{RCL,IM}}$. This power loss term is caused by the joule losses occurring in the rotor windings of the IM. Since the IPMSM is embedded with rotor permanent magnets, there are no rotor windings and, hence, $P_{\text{RCL,IM}}$ is absent in IPMSMs.

The IM model is adopted to compute the electric generator efficiency and exergy terms from Eqs. (9) and (11), respectively. From now on, we refer to quantities related to the generator with the subscript *gen*. The speed-torque map of the generator efficiency and exergy destruction at 25 °C are shown in Figs. 4 and 5, respectively. This is the first time that the exergetic static behavior of an electric machine is described by a speed-torque map. The exergy destruction map enables to quantify the generator irreversibilities that cannot be obtained from the energetic efficiency map. The representation of the generator exergy destruction on the speed-torque plane clarifies that the irreversibilities of the generator increase along with the generator power. Moreover, increases in generator torque lead to higher exergy destruction, due to the higher power losses.

2.6 Internal Combustion Engine. The ICE is characterized by a steady-state instantaneous fuel consumption $\dot{m}_f$ map, which is a

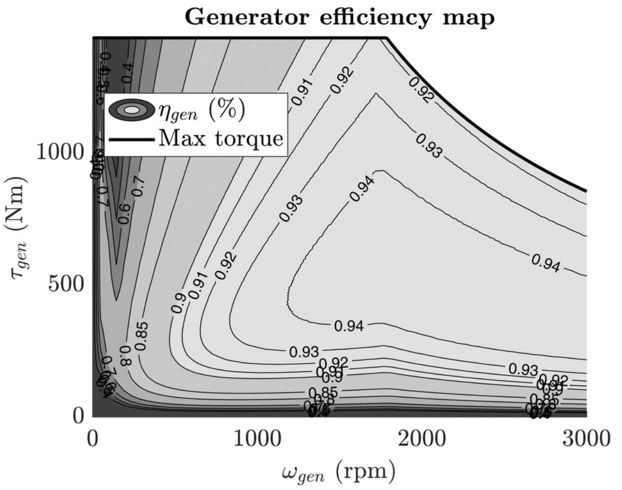

Fig. 4 Efficiency map of the generator at the temperature $T_{\text{gen}} = 25\,^\circ\text{C}$

function of the engine speed ω_{eng} and torque τ_{eng}. The output engine power P_{eng} is calculated as $P_{\text{eng}} = \frac{P_{\text{gen}}}{\eta_{\text{gen}}}$, where η_{gen} is the generator efficiency. The exergetic model of the ICE is built upon the mean-value exergetic modeling framework developed in the previous work [24]. Each ICE exergy rate term can be expressed as a function of ω_{eng} and τ_{eng}. The exergy destruction rate $\dot{X}_{\text{dest,eng}}$ is calculated as a summation of the following: $\dot{X}_{\text{dest,eng}} = \dot{X}_{\text{comb,eng}} + \dot{X}_{\text{fric,eng}} + \dot{X}_{\text{others,eng}}$, where $\dot{X}_{\text{comb,eng}}$, $\dot{X}_{\text{fric,eng}}$ and $\dot{X}_{\text{others,eng}}$ account for combustion irreversibilities, mechanical losses related to friction, and the exergy destruction of unmodeled phenomena, respectively. The exergy transfer terms of the ICE are: $\dot{X}_{\text{heat,eng}}$ due to the heat exchange between in-cylinder mixture and cylinder's walls, $\dot{X}_{\text{exh,eng}}$ related to the exhaust gases, the fuel exergy term $\dot{X}_{\text{fuel,eng}}$, and the intake air exergy flow $\dot{X}_{\text{intk,eng}}$. The fuel exergy rate $\dot{X}_{\text{fuel,eng}}$ is proportional to the instantaneous fuel consumption $\dot{m}_f$ through

$$\dot{X}_{\text{fuel,eng}} = (1.04224 + 0.011925x/y - 0.042/x)\text{LHV}\dot{m}_f \tag{12}$$

where LHV is the fuel lower heating value, while x and y define the fuel chemical composition (C_xH_y). The mathematical formulation of each ICE exergy term is shown in Table 1. The physical quantities required for computing the ICE exergy terms are calculated through the mean-value ICE model from Ref. [24]. This approach allows to quantify offline the required quantities, such as the in-cylinder gas temperature T_{cyl}, in-cylinder gas pressure P_{cyl}, and in-cylinder gas to wall thermal exchange $\dot{Q}_{\text{cyl}}$, as a function of the operating point and without the use of expensive sensors onboard.

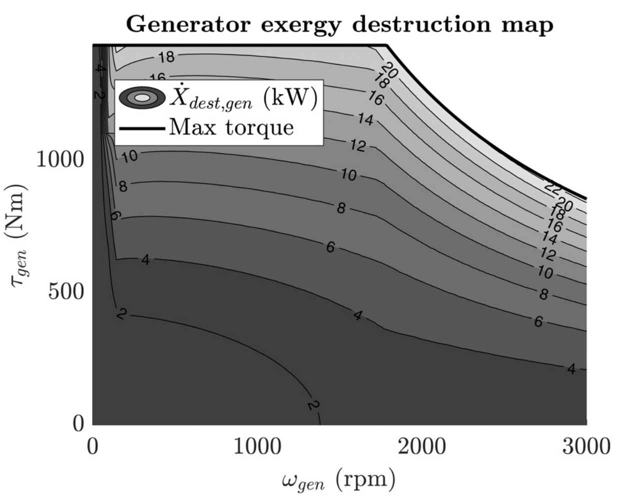

Fig. 5 Exergy destruction map of the generator at the temperature $T_{\text{gen}} = 25\,^\circ\text{C}$

Table 1 ICE exergy model [24]

Intake air

$$\dot{X}_{\text{intk,eng}} = \sum_{\sigma\in S} n_{\text{I},\sigma}\left(\psi^{\text{I}}_{\text{ch},\sigma} + \psi^{\text{I}}_{\text{ph},\sigma}\right), \quad S = \{\text{N}_2, \text{CO}_2, \text{H}_2\text{O}, \text{O}_2\}$$

$$n_{I,\sigma} = \dot{n}_I f^I_\sigma$$

$$\psi^I_{\text{ph},\sigma} = (h_\sigma(T_I) - T_0 s_\sigma(T_I)) - (h^*_\sigma(T_0) - T_0 s^*_\sigma(T_0))$$

$$\psi^I_{\text{ch},\sigma} = R_{\text{gas}} T_0 \log\left(\frac{f^I_\sigma}{f_{\sigma,0}}\right)$$

Mechanical work

$$\dot{X}_{\text{work,eng}} = -P_{\text{eng}}$$

Heat exchange

$$\dot{X}_{\text{heat,eng}} = \left(1 - \frac{T_0}{T_{\text{cyl}}}\right)\left(-\dot{Q}_{\text{cyl}}\right)$$

Exhaust gas

$$\dot{X}_{\text{exh,eng}} = -\sum_{\sigma\in S} \dot{n}_{E,\sigma}\left(\psi^E_{\text{ch},\sigma} + \psi^E_{\text{ph},\sigma}\right)$$

$$\dot{n}_{E,\sigma} = \dot{n}_E f^E_\sigma$$

$$\psi^E_{\text{ph},\sigma} = (h_\sigma(T_E) - T_0 s_\sigma(T_E)) - (h^*_\sigma(T_0) - T_0 s^*_\sigma(T_0))$$

$$\psi^E_{\text{ch},\sigma} = R_{\text{gas}} T_0 \log\left(\frac{f^E_\sigma}{f_{\sigma,0}}\right)$$

Combustion irreversibilities

$$\begin{aligned}\dot{X}_{\text{comb,eng}} = &-\frac{T_0}{T_{\text{cyl}}}\left(g_f - x g_{\text{CO}_2} - \frac{y}{2} g_{\text{H}_2\text{O}} + \left(x + \frac{y}{4}\right) g_{\text{O}_2}\right)\dot{n}_f \\ &- \frac{T_0}{T_{\text{cyl}}}\frac{\lambda}{1 - x_{\text{EGR}}}\left(x + \frac{y}{4}\right) 3.76 R_{\text{gas}} T_{\text{cyl}} \log\left(\frac{f^{\text{I}}_{N_2}}{f^{\text{E}}_{N_2}}\right)\dot{n}_f \\ &- \frac{T_0}{T_{\text{cyl}}} R_{\text{gas}} T_{\text{cyl}} \sum_{\sigma\in S\setminus\{N_2\}}\left[\nu^{\text{I}}_\sigma \log\left(\frac{f^{\text{I}}_\sigma P_{\text{cyl}}}{P_0}\right) - \nu^{\text{E}}_\sigma \log\left(\frac{f^{\text{E}}_\sigma P_{\text{cyl}}}{P_0}\right)\right]\dot{n}_f\end{aligned}$$

Frictions

$$\dot{X}_{\text{fric,eng}} = -\frac{\omega_{\text{eng}}}{4\pi}\text{FMEP} \cdot V_{d,\text{tot}}$$

$$\text{FMEP} = 1000\left(C_1 + C_2\omega_{\text{eng}} + C_3 S^2_p\right)$$

Others

$$\begin{aligned}\dot{X}_{\text{others}} = &-\left[\dot{X}_{\text{fuel,eng}} + \dot{X}_{\text{intk,eng}} + \dot{X}_{\text{work,eng}} + \dot{X}_{\text{heat,eng}} + \dot{X}_{\text{exh,eng}}\right] \\ &-\left[\dot{X}_{\text{comb,eng}} + \dot{X}_{\text{fric,eng}}\right]\end{aligned}$$

2.7 Exergy Balance of the Genset. According to Ref. [22], the ICE dominates the exergy loss and destruction in a HEV. The ICE and generator are lumped in a genset that accounts for the exergy loss and destruction of both components. The genset exergy balance is carried out in this section and used later in Sec. 3 for the formulation of the ExMSs, which aim to minimize genset exergetic terms. The genset exergy balance is formulated by considering a representative

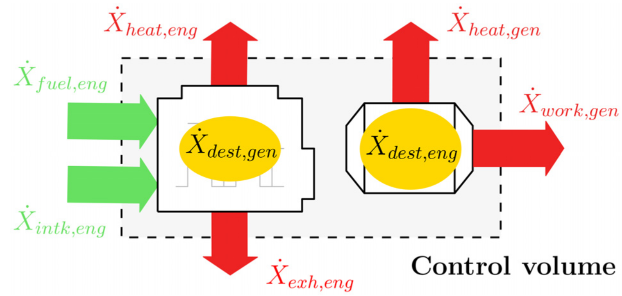

Fig. 6 Exergy balance of the genset system

control volume and the heat, work, and mass crossing its boundaries (see Fig. 6) as $\dot{X}_{\text{genset}} = \dot{X}_{\text{in,genset}} - \dot{X}_{\text{out,genset}} + \dot{X}_{\text{dest,genset}}$, where $\dot{X}_{\text{genset}}$ is the exergy of the genset, $\dot{X}_{\text{in,genset}}$ and $\dot{X}_{\text{out,genset}}$ are the exergy transfer terms modeling heat, work, and mass fluxes entering and leaving the control volume enclosing the genset and $\dot{X}_{\text{dest,genset}}$ is the exergy destroyed. The exergy transfer entering the control volume can be expressed as $\dot{X}_{\text{in,genset}} = \dot{X}_{\text{fuel,eng}} + \dot{X}_{\text{intk,eng}}$. The exergy destruction of the whole system is the sum of the exergy destruction of ICE and generator, i.e., $\dot{X}_{\text{dest,genset}} = \dot{X}_{\text{dest,eng}} + \dot{X}_{\text{dest,gen}}$. Finally, the exergy transfer leaving the control volume accounts for the exergy terms related to exhaust gases $\dot{X}_{\text{exh,eng}}$, ICE and generator heat exchange ($\dot{X}_{\text{heat,eng}}$ and $\dot{X}_{\text{heat,gen}}$, respectively), and generator work $\dot{X}_{\text{work,gen}}$, i.e., $\dot{X}_{\text{out,genset}} = \dot{X}_{\text{exh,eng}} + \dot{X}_{\text{heat,eng}} + \dot{X}_{\text{heat,gen}} + \dot{X}_{\text{work,gen}}$

3 Exergy Management Problem

The exergy management problem is formulated as a constrained optimal control problem over the fixed time interval $[t_0,t_f]$

$$\begin{aligned} \underset{P_{\text{batt}}}{\text{minimize}} \quad & J = \int_{t_0}^{t_f} c_r\left(P_{\text{mot},e}(t), P_{\text{batt}}(t), \mathbf{x}(t)\right)dt \\ \text{subject to} \quad & \dot{\mathbf{x}}(t) = F\left(P_{\text{mot},e}(t), P_{\text{batt}}(t), \mathbf{x}(t)\right) \\ & g_j\left(P_{\text{mot},e}(t), P_{\text{batt}}(t), \mathbf{x}(t)\right) \le 0, \forall g_j \in G \end{aligned} \tag{13}$$

where t_0 and t_f are the initial and final time instants of the driving mission, c_r is the running cost, P_{batt} is the control variable, $\mathbf{x}$ is the state vector, $\dot{\mathbf{x}}(t) = F(P_{\text{mot},e}(t), P_{\text{batt}}(t), \mathbf{x}(t))$ are the state dynamics, and G is the set of global and local constraints. The electrical power required by the electric traction motors $4 \cdot P_{\text{mot},e}$ is the exogenous input. In this section, three different exergy-based management strategies and their respective OCPs are formulated. All control problems share the same state dynamics and constraints, but different cost functions.

3.1 Cost Functions. To exploit the advantages of the exergetic analysis over the energetic one, new exergetic optimization targets are formulated. The ExMSs formulated in this section make use of genset exergetic terms which are not available in classical energetic methods.

3.1.1 Energy Management Strategy. First, the standard EMS is introduced as a benchmark for comparison purposes. The cost function of the EMS optimal control problem (OCP_{EMS}) is the fuel consumption rate $\dot{m}_f$

$$J_{\text{EMS}} = \int_{t_0}^{t_f} \dot{m}_f(t, P_{\text{batt}}, T_{\text{gen}})dt \tag{14}$$

It is worth noting that the instantaneous fuel consumption can be written as a function of the exergy term related to fuel from Eq. (12): $\dot{m}_f = \frac{\dot{X}_{\text{fuel,eng}}}{(1.04224+0.011925x/y-0.042/x)\text{LHV}}$. The same solutions could be obtained by adopting $\dot{X}_{\text{fuel,eng}}$ as running cost.

3.1.2 Minimization of Exergy Destruction. The goal of the optimal control problem ($\text{OCP}_{\text{ExMS},1}$) is the reduction of the genset's irreversibilities through the cost function $J_{\text{ExMS},1}$ which quantifies the exergy destruction of the whole genset system

$$J_{\text{ExMS},1} = \int_{t_0}^{t_f} |\dot{X}_{\text{dest,genset}}(t, P_{\text{batt}}, T_{\text{gen}})|dt \tag{15}$$

where $\dot{X}_{\text{dest,genset}}(t, P_{\text{batt}}, T_{\text{gen}})$ is always negative, since the exergy destruction reduces the system's available work and, consequently, the exergy.

3.1.3 Minimization of Thermal Emissions. Low thermal emissions are crucial in military applications to keep the vehicle undetected [23]. Specifically, the powertrain component at the highest temperature is the one that can be detected more easily by thermal imaging. The cost function $J_{\text{ExMS},2}$ used in the optimal control problem ($\text{OCP}_{\text{ExMS},2}$) quantifies the exergy transfer related to heat emissions of the genset and takes the following form:

$$\begin{aligned} J_{\text{ExMS},2} &= \int_{t_0}^{t_f} |\dot{X}_{\text{heat,genset}}|dt \\ \dot{X}_{\text{heat,genset}} &= \min(\dot{X}_{\text{heat,eng}}(t, P_{\text{batt}}, T_{\text{gen}}), \dot{X}_{\text{heat,gen}}(t, P_{\text{batt}}, T_{\text{gen}})) \end{aligned} \tag{16}$$

3.2 State Dynamics and Constraints. The state variables considered in this study are the SOC and the generator temperature T_{gen}, whose dynamics are written as follows:

$$\begin{aligned} \dot{\mathbf{x}}(t) &= F\left(P_{\text{mot},e}(t), P_{\text{batt}}(t), \mathbf{x}(t)\right) \\ &= \begin{bmatrix} \dot{\text{SOC}}(P_{\text{batt}}(t), \mathbf{x}(t)) \\ \dot{T}_{\text{gen}}\left(P_{\text{mot},e}(t), P_{\text{batt}}(t), \mathbf{x}(t)\right) \end{bmatrix} \\ &= \begin{bmatrix} -\dfrac{I_{\text{batt}}(P_{\text{batt}}(t), \mathbf{x}(t))}{Q_{\text{batt}}} \\ \dfrac{\dot{Q}_{\text{heat,gen}}(\mathbf{x}(t)) + P_{\text{loss,gen}}\left(P_{\text{mot},e}(t), P_{\text{batt}}(t), \mathbf{x}(t)\right)}{C_{\text{gen}}} \end{bmatrix} \end{aligned} \tag{17}$$

The EMS and ExMSs are subject to several global and local constraints. Battery charge sustaining is enforced through the following global constraint, $\text{SOC}(t_f) = \text{SOC}(t_0)$. Other local constraints related to state and control variables need to be satisfied at each time $t \in [t_0,t_f]$

$$\begin{aligned} I_{\text{cell,min}} &< I_{\text{cell}}(t) < I_{\text{cell,max}}, \\ P_{\text{gen,min}} &< P_{\text{gen}}(t) < P_{\text{gen,max}}, \\ P_{\text{eng,min}} &< P_{\text{eng}}(t) < P_{\text{eng,max}}, \\ \text{SOC}_{\text{min}} &< \text{SOC}(t) < \text{SOC}_{\text{max}}, \\ T_{\text{gen}}(t) &< T_{\text{gen,max}} \end{aligned} \tag{18}$$

where $P_{\text{gen,min}}$, $P_{\text{gen,max}}$, $P_{\text{eng,min}}$, and $P_{\text{eng,max}}$ are the minimum and maximum power of generator and ICE, respectively; the cell current I_{cell} is limited by the minimum and maximum threshold $I_{\text{cell,min}}$ and $I_{\text{cell,max}}$. The constraints on the state variables allow to maintain the SOC in the desired range $[\text{SOC}_{\text{min}}, \text{SOC}_{\text{max}}]$ and force the generator to operate at a temperature lower than the maximum limit $T_{\text{gen,max}}$. Considering a generator insulation of class B[3] [37], $T_{\text{gen,max}}$ is equivalent to 130 °C.

3.3 Dynamic Programming. The optimal control problems are solved through Dynamic Programming (DP), which relies on Bellman's principle of optimality [38]. Bellman's principle states that the solution from any intermediate state of the optimal solution to the final state is also optimal [39]. This fact is exploited in DP by proceeding backward in time beginning from the final state and searching for the optimal solution through all possible discretized values of state and control variables. The driving cycle must therefore be known a priori, which requires the use of a backward discretized vehicle model.

The DP algorithm is implemented through the MATLAB function developed in [40]. The discretization grids of the two state variables ΔSOC and ΔT_{gen} and control variable ΔP_{batt} are carefully chosen to avoid numerical instability: $\Delta\text{SOC} = 0.01\%$, $\Delta T_{\text{gen}} = 1\,°\text{C}$, and $\Delta P_{\text{batt}} = 100$ W.

[3]There are typically four insulation classes for IMs (A,B,F,H) [37], each indicating the highest winding temperature the insulation material can withstand.

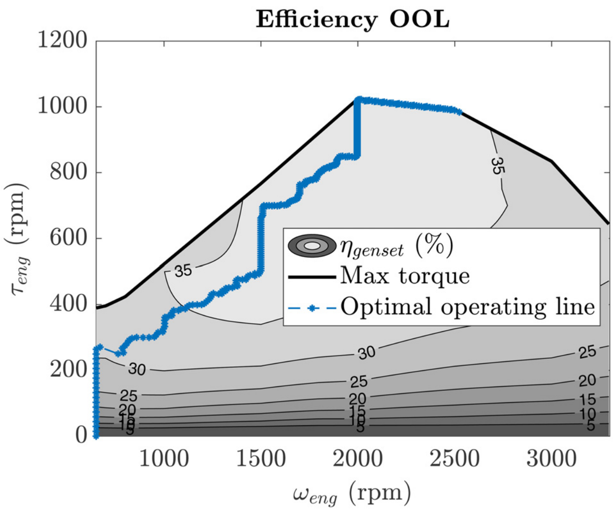

Fig. 7 Efficiency map and optimal operating line for EMS at $T_{gen} = 25\,^\circ$C

3.4 Optimal Operating Lines. A power request P_{eng} can be actuated at different operating points (ω_{eng},τ_{eng}) of the ICE. For each strategy, an optimal operating line (OOL) can be defined so that, given a certain power request, the best working point is selected among all the possible tuples (ω_{eng}, τ_{eng}) [29]. In Appendix B, the procedure to determine the optimal operating lines is explained. For the EMS, the optimal operating line in Fig. 7 is designed to maximize the efficiency η_{genset} of the genset: $\eta_{genset} = \frac{P_{gen}}{LHV \cdot \dot{m}_f}$, where LHV is the fuel lower heating value.

The optimal operating line related to the first ExMS (15) is designed to minimize the genset exergy destruction $\dot{X}_{dest,genset}$. The ICE map and operating line are shown at the temperature $T_{gen} = 25\,^\circ$C in Fig. 8. The operating lines related to the EMS and ExMS for minimization of exergy destruction are located in similar ICE operating regions.

For the minimization of thermal emissions (16), the optimal line (shown in Fig. 9) is designed to minimize the exergy transfer due to the heat exchange between the ICE and the surroundings. It is worth noting that the optimal operating points for this strategy are located at higher speeds compared to the previous strategies. As a matter of fact, for a given engine power, the in-cylinder gas to wall heat transfer increases with torque mainly due to the increasing in-cylinder gas temperature T_{cyl} [41]. The selection of high-speed operating points allows to reduce the gas temperature (Appendix C) and, consequently, the heat exchange between the cylinder and the environment. Recalling Sec. 2, the running costs $\dot{m}_f$, $\dot{X}_{dest,genset}$, and $\dot{X}_{heat,genset}$ are functions of the generator operating point (ω_{gen},τ_{gen}) and the generator temperature T_{gen}. Once the optimal operating line is selected, $\dot{m}_f$, $\dot{X}_{dest,genset}$, and $\dot{X}_{heat,genset}$ can be expressed as a function of P_{gen} and T_{gen}.

3.5 Polynomial Approximation of the Cost Functions. Generally speaking, an optimal control policy (either from an energy or exergy standpoint) might not lead to good drivability [42]. Indeed, the DP optimal control policy can result in abrupt variations of the engine power between consecutive time steps. However, the chattering behavior of the ICE power must be avoided since it can cause undesirable powertrain noise, vibration, and harshness [43]. The numerical instabilities causing the chattering behavior can be avoided by approximating the running costs $\dot{m}_f$, $\dot{X}_{dest,genset}$, and $\dot{X}_{heat,genset}$ with polynomial functions of the delivered generator power P_{gen}. However, since the running costs are functions of both P_{gen} and T_{gen}, this approximation can only be performed at a fixed T_{gen}. Hence, n_T equally spaced temperature values, referred to as node temperatures, are selected between the environment temperature and the maximum generator temperature. The running costs $\dot{m}_f$, $\dot{X}_{dest,genset}$, and $\dot{X}_{heat,genset}$ are approximated as a polynomial function of P_{gen} for each node temperature through the `polyfit` MATLAB function. Linear interpolation is used to determine the value of the running cost associated with a temperature different from any node temperature. In this work, the number n_T of node temperatures is selected equal to 12.

The root-mean-square percentage error (RMSE) is used to quantify the error between the real cost and the approximated one. Based on this metric, the 3rd, 3rd, and 10th degrees of the polynomial functions are selected to obtain 2.50%, 3.66%, and 2.43% RMSEs to approximate $\dot{m}_f$, $\dot{X}_{dest,genset}$, and $\dot{X}_{heat,genset}$, respectively. Figures 10–12 show the $\dot{m}_f$, $\dot{X}_{dest,genset}$, and $\dot{X}_{heat,genset}$ and their polynomial approximation as functions of P_{gen} at $T_{gen} = 25\,^\circ$C.

4 Results

The ExMS problems are solved for the military vehicle model described in Sec. 2. The values of parameters of the vehicle and powertrain components are reported in Table 2. Two driving missions, shown in Fig. 13, have been used to solve the proposed ExMS problems: Munson without road slope and Munson with road

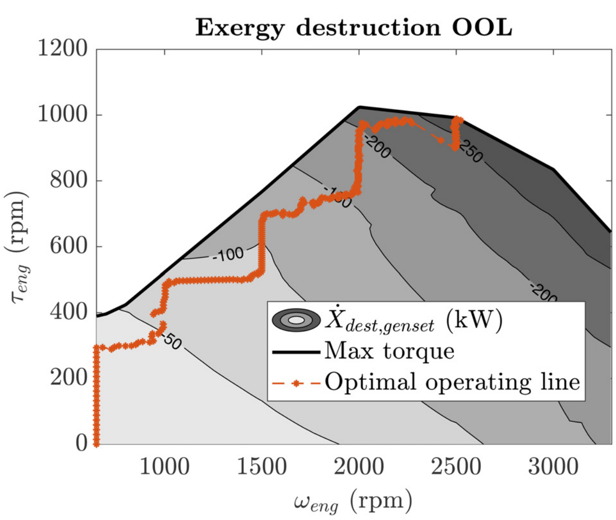

Fig. 8 Exergy destruction map and optimal operating line for minimization of exergy destruction ExMS at $T_{gen} = 25\,^\circ$C

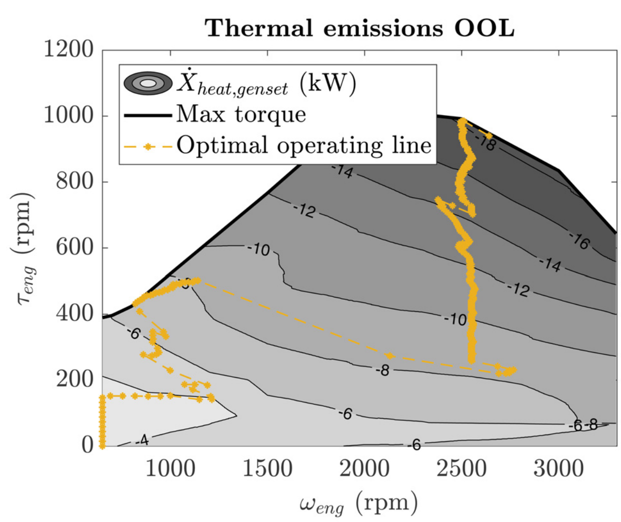

Fig. 9 Exergy transfer due to the heat exchange and optimal operating line for minimization of thermal emissions ExMS at $T_{gen} = 25\,^\circ$C

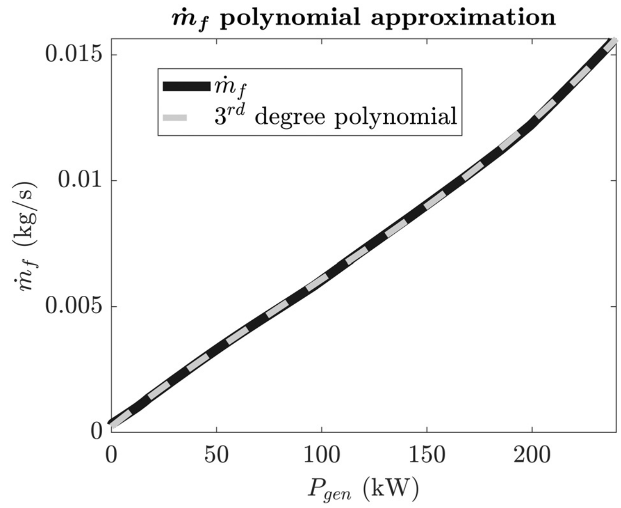

Fig. 10 $\dot{m}_f$ map as a function of P_{gen} and its polynomial approximation at $T_{gen} = 25\,^\circ\mathrm{C}$

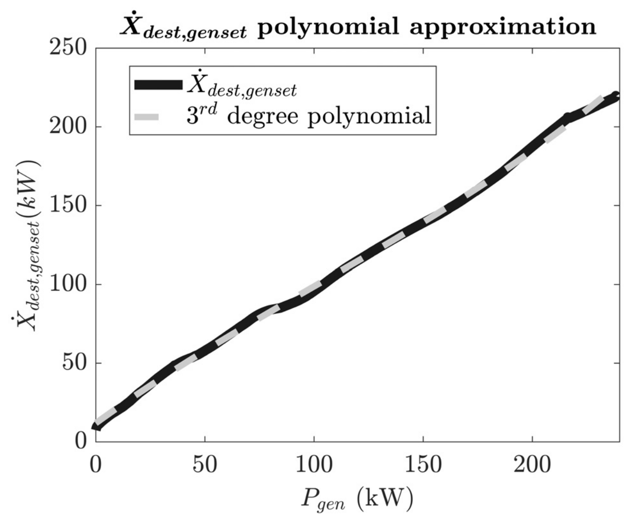

Fig. 11 $\dot{X}_{dest,genset}$ map as a function of P_{gen} and its polynomial approximation at $T_{gen} = 25\,^\circ\mathrm{C}$

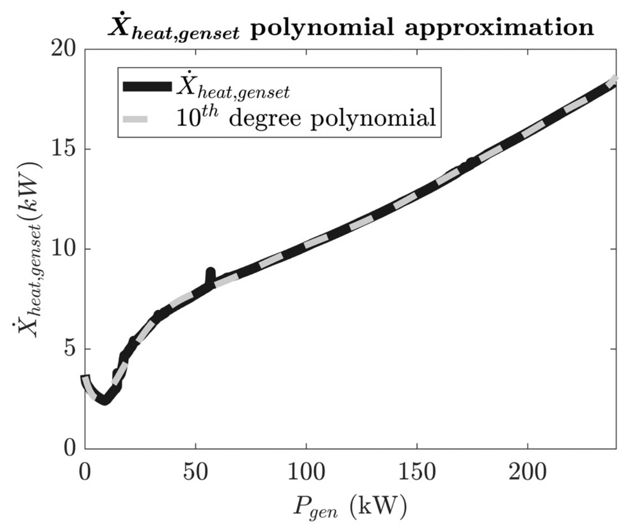

Fig. 12 $\dot{X}_{heat,genset}$ map as a function of P_{gen} and its polynomial approximation at $T_{gen} = 25\,^\circ\mathrm{C}$

Table 2 Vehicle specifications

Parameter	Unit	Value
ρ_a	1.2	kg/m^3
g	9.81	m/s^2
R_w	0.59 [44]	m
M	13,430	kg
C_r	0.01 [44]	—
C_x	0.7 [44]	—
A	5.72 [44]	m^2
η_{GB}	1	—
C_{mot}	29,126 [22]	J/K
$h_{\mathrm{out,mot}}$	54.64 [22]	W/K
N_S	124	—
N_P	5	—
Q_{cell}	4.85 [31]	Ah
C_{cell}	156.4 [31]	J/K
$h_{\mathrm{out,cell}}$	0.2085 [31]	W/K
$f_{\mathrm{gen,nom}}$	60 [45]	Hz
$V_{\mathrm{gen,nom}}$	460 [45]	V
n_P	4 [45]	—
$R_{1,0}$	0.0088 [45]	Ω
$R_{2,0}$	0.0383 [45]	Ω
R_C	100	Ω
X_1	0.0431 [45]	Ω
X_2	0.0431 [45]	Ω
X_M	2.0358 [45]	Ω
C_{gen}	29,126 [22]	J/K
$h_{\mathrm{out,gen}}$	54.64 [22]	W/K
c_{fric}	0.06346 [46]	Nms

slope. The first mission is a simple driving cycle with constant velocity and no slope. Despite its simplicity, it is crucial to test the ExMSs on this cycle to check for the presence of numerical instabilities. Since the mission is characterized by a constant velocity profile, the power requested at the wheels P_w is constant for almost the whole driving mission. Therefore, the presence of a chattering behavior of the generator power would be an indicator of numerical instabilities. The second cycle Munson with slope is a realistic military driving mission with a constant velocity profile and variable slope.

Another crucial factor to consider for military vehicles is the power needed by auxiliary systems onboard [47]. Therefore, the Munson with road slope is tested without auxiliary power ($P_{\mathrm{aux}} = 0\,\mathrm{kW}$) and with continuous auxiliary power ($P_{\mathrm{aux}} = 40\,\mathrm{kW}$)

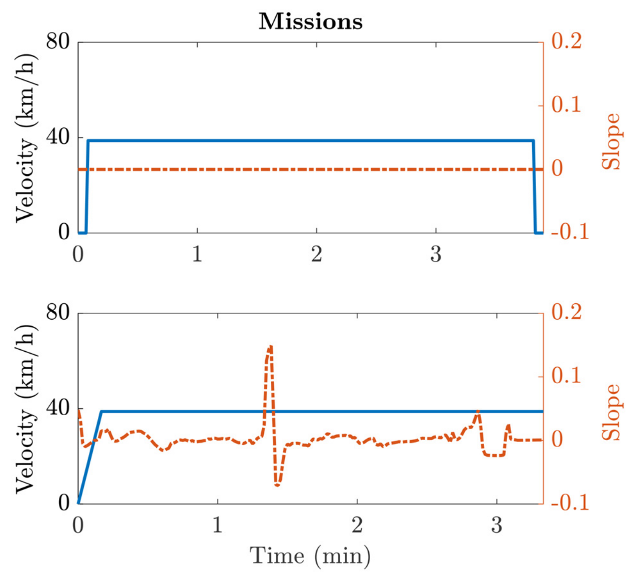

Fig. 13 Velocity and slope profiles of the driving missions: Munson without road slope, and Munson with road slope

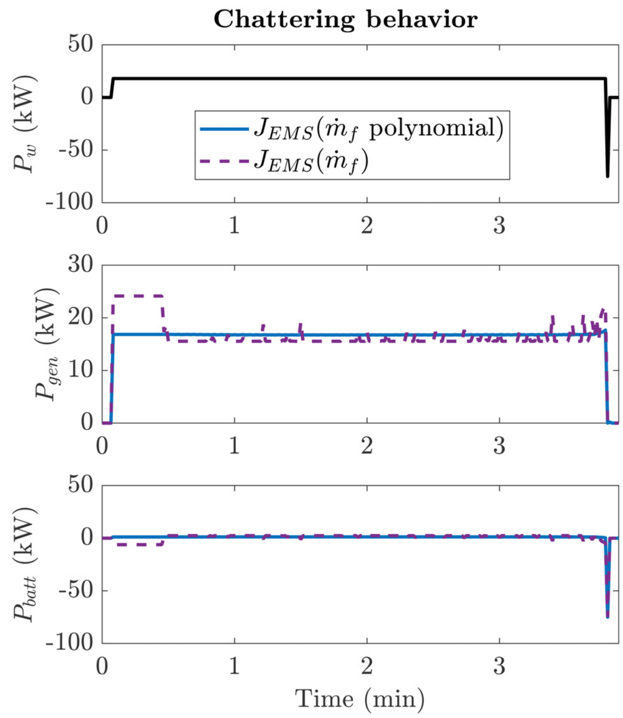

Fig. 14 Power requested at the wheels, generator, and battery optimal power profiles for J_{EMS} with and without $\dot{m}_f$ polynomial approximation over the Munson without slope mission

to assess how the presence of auxiliaries affects the results. Moreover, the time-step is chosen to be 1 s as done in previous energy management works with DP, e.g., Refs. [40] and [48]. Before analyzing the results obtained by the control strategies over the driving missions, the effect of the polynomial approximation of the running cost on the results is assessed. In Fig. 14, the optimal power

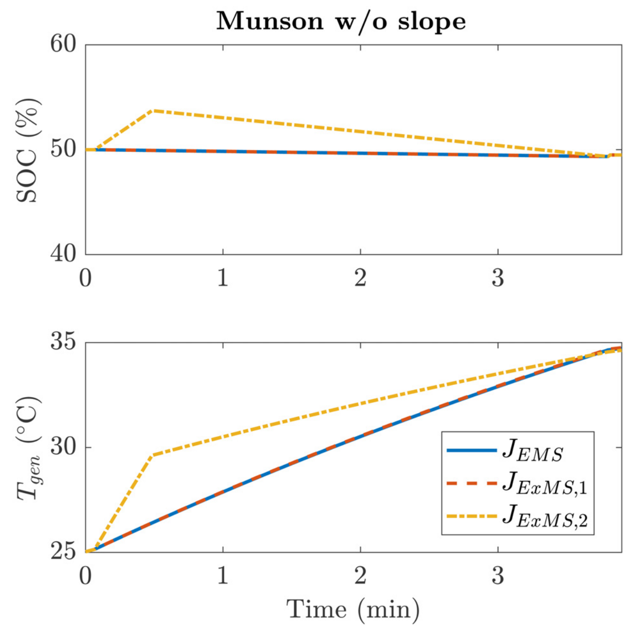

Fig. 16 SOC and generator temperature profiles for J_{EMS}, $J_{\mathrm{ExMS,1}}$, and $J_{\mathrm{ExMS,2}}$ over the Munson without slope mission

splits obtained by the EMS with and without the polynomial approximation of the running cost are shown. The EMS without polynomial approximation displays a chattering behavior of the generator power. On the other hand, the use of the polynomial approximation of the running cost enables to avoid the undesired high-frequency variations of the generator power. Therefore, the results shown in the remainder of this section are obtained with the polynomial approximation of the running costs to avoid the chattering behavior. Starting with the Munson without road slope, the optimal power splits and state dynamics for the different ExMSs

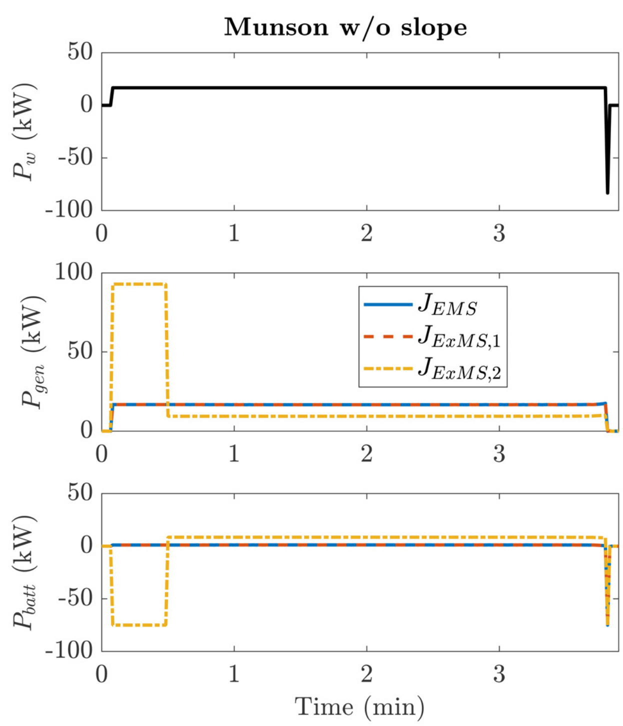

Fig. 15 Power requested at the wheels, generator, and battery optimal power profiles for J_{EMS}, $J_{\mathrm{ExMS,1}}$, and $J_{\mathrm{ExMS,2}}$ over the Munson without slope mission

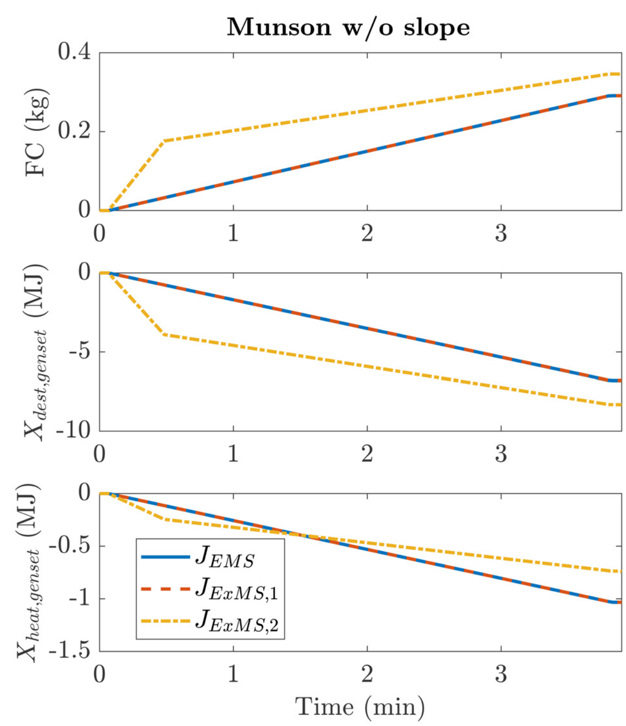

Fig. 17 Cumulative FC, exergy destruction, and exergy related to heat for J_{EMS}, $J_{\mathrm{ExMS,1}}$, and $J_{\mathrm{ExMS,2}}$ over the Munson without slope mission

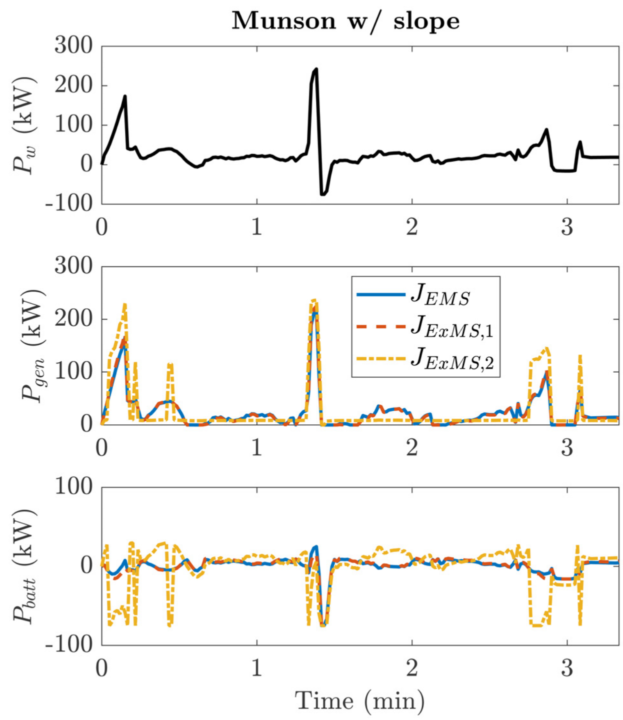

Fig. 18 Power requested at the wheels, generator, and battery optimal power profiles for J_{EMS}, $J_{\mathrm{ExMS,1}}$, and $J_{\mathrm{ExMS,2}}$ over the Munson with slope mission with no auxiliary power

are shown in Figs. 15 and 16, respectively. It is worth noting that P_w is the same for all the different control strategies over the same driving cycle. On the other hand, the generator and battery power profiles, shown in the second and third subplots of Fig. 15, are generated by the optimal DP solution to the specific optimization problem and are different for each management strategy. Interestingly, the EMS[4] and the ExMS for minimization of exergy destruction lead to almost identical power splits over the Munson without slope mission, maintaining the generator and battery power constant for almost the whole simulation. The similarities between the control policy of the two strategies can be explained by the fact that the ExMS for minimization of exergy destruction aims to minimize the irreversibilities, which is comparable to the EMS implicit minimization of system inefficiencies to reduce fuel consumption. This explanation is in line with the results of previous studies [49] in the field of aircraft optimization. On the other hand, $J_{\mathrm{ExMS,2}}$ shows a different behavior. The DP algorithm selects high generator power P_{gen} to charge the battery at the beginning of the mission, as shown by the initial SOC increase in Fig. 16, and then, P_{gen} is settled around 10 kW to operate close to the minimum of the thermal emission curve (shown in Fig. 12). The generator temperature T_{gen} trend, shown in the second subplot of Fig. 16, is correlated to the generator power profile: the higher the P_{gen}, the higher the temperature variation. Moreover, the absence of chattering behavior in the optimal power profiles demonstrates that the numerical solution is stable.

Fuel consumption, exergy destruction, and exergy transfer due to heat exchange of the genset system need to be evaluated to assess the performance of the different ExMSs. Figure 17 shows that the EMS and the ExMS for minimization of exergy destruction hold almost identical performances, achieving a reduction of fuel consumption (18.9%) and exergy destruction (18.3%) with respect to the thermal emissions strategy. On the other hand, $J_{\mathrm{ExMS,2}}$ achieves substantially lower thermal emissions than J_{EMS} and $J_{\mathrm{ExMS,1}}$ (around 28.7%), proving that the ExMS for minimization of thermal emissions is the

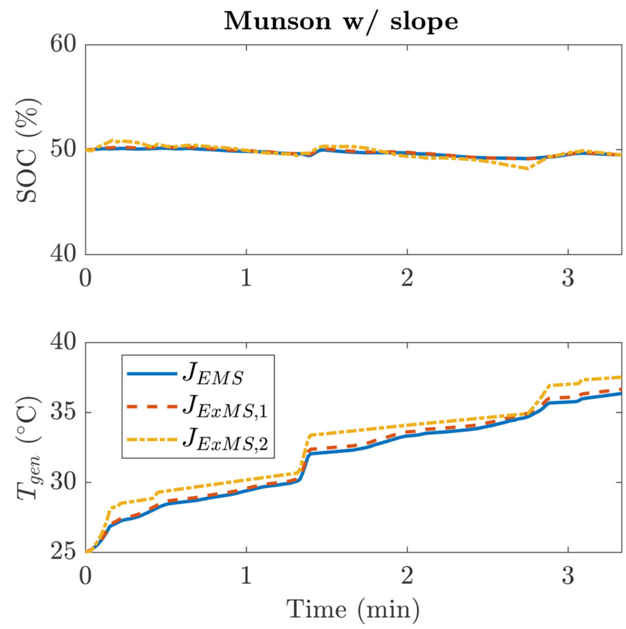

Fig. 19 SOC and generator temperature profiles for J_{EMS}, $J_{\mathrm{ExMS,1}}$, and $J_{\mathrm{ExMS,2}}$ over the Munson with slope mission with no auxiliary power

most effective strategy to avoid detection from thermal imaging. When examining the Munson with road slope, the distinction between the ExMSs and the standard EMS becomes more evident. In particular, the generator and battery profiles, and the state dynamics, shown in Figs. 18 and 19, respectively, are slightly different for J_{EMS} and $J_{\mathrm{ExMS,1}}$. In line with the results from the first driving mission, $J_{\mathrm{ExMS,2}}$ exhibits a significantly distinct behavior from J_{EMS} and $J_{\mathrm{ExMS,1}}$. While the generator power profiles of J_{EMS} and $J_{\mathrm{ExMS,1}}$ have trends similar to the power requested at the wheels, the ExMS for the

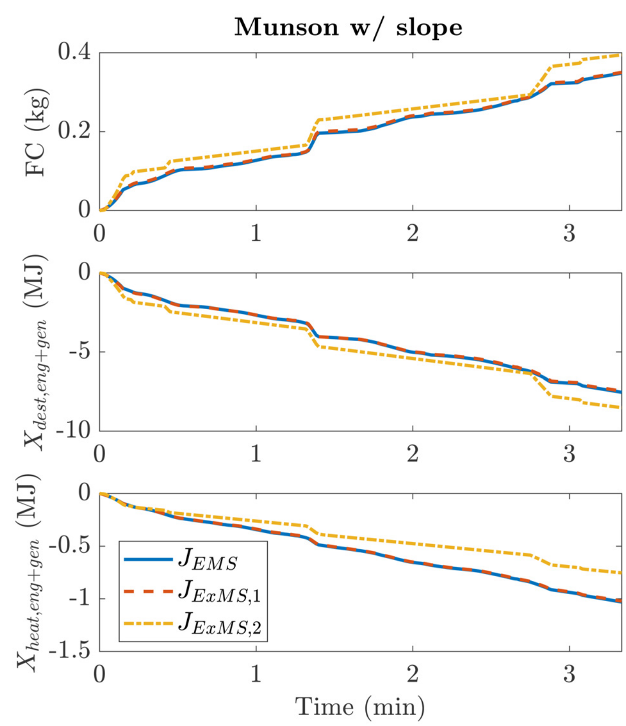

Fig. 20 Cumulative FC, exergy destruction, and exergy related to heat for J_{EMS}, $J_{\mathrm{ExMS,1}}$, and $J_{\mathrm{ExMS,2}}$ over the Munson with slope mission with no auxiliary power

[4]In this section, the cost function symbols J_{EMS}, $J_{\mathrm{ExMS,1}}$ and $J_{\mathrm{ExMS,2}}$ refer to the solutions to the $\mathrm{OCP_{EMS}}$, $\mathrm{OCP_{ExMS,1}}$, and $\mathrm{OCP_{ExMS,2}}$, respectively

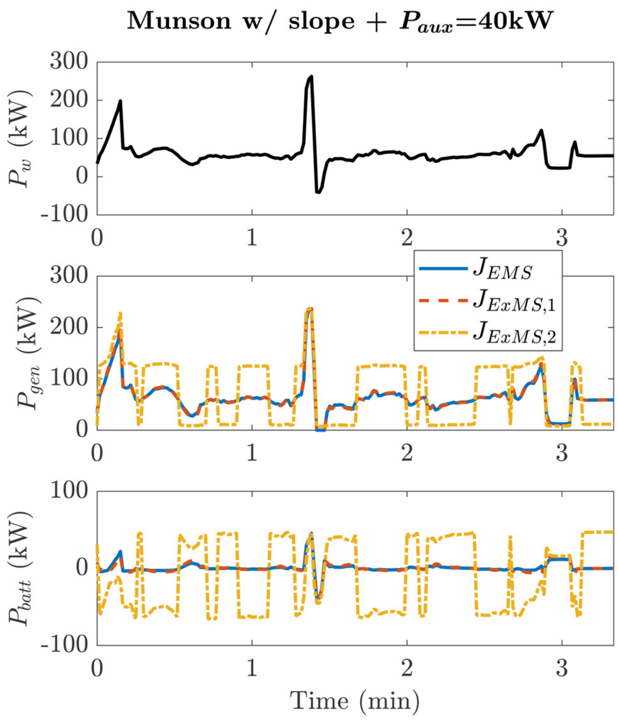

Fig. 21 Power requested at the wheels, generator, and battery optimal power profiles for J_{EMS}, $J_{\mathrm{ExMS,1}}$, and $J_{\mathrm{ExMS,2}}$ over the Munson with slope mission with auxiliary power

minimization of thermal emissions tends to select different P_{gen}. In particular, P_{gen} lower than 8 kW are always avoided in $J_{\mathrm{ExMS,2}}$ to minimize the exergy transfer due to heat exchange as shown in Fig. 12, and high powers are selected to operate the ICE at a high speed. The high-speed rotation of the ICE allows to reduce the in-cylinder gas temperature, consequently decreasing the exergy transfer due to the heat exchange between the ICE and the environment. Even though this second driving mission is more dynamic than the first one, no ExMS causes the generator temperature to exceed 40 °C, as shown in the second subplot of Fig. 19. Interestingly, compared to the other strategies, the ExMS for minimization of thermal emissions leads to the highest generator temperature. This apparently counterintuitive result is explained by the fact that the magnitude of the exergy transfer due to heat exchange between the ICE and the environment $|\dot{X}_{\mathrm{heat,eng}}|$ is higher than the magnitude of the exergy transfer due to heat exchange between the generator and the environment $|\dot{X}_{\mathrm{heat,gen}}|$ for every operating point. Indeed, the minimum value of $|\dot{X}_{\mathrm{heat,eng}}|$ (2.4 kW) is higher than the maximum value of $|\dot{X}_{\mathrm{heat,gen}}|$ (1.5 kW), which can be calculated from Eq. (11) considering the maximum generator temperature $T_{\mathrm{gen,max}}$. Therefore, the running cost $|\dot{X}_{\mathrm{heat,genset}}|$ is always equal to $|\dot{X}_{\mathrm{heat,eng}}|$, and the ExMS for minimization of thermal emissions always aims to minimize $|\dot{X}_{\mathrm{heat,eng}}|$, disregarding $|\dot{X}_{\mathrm{heat,gen}}|$, and the generator temperature.

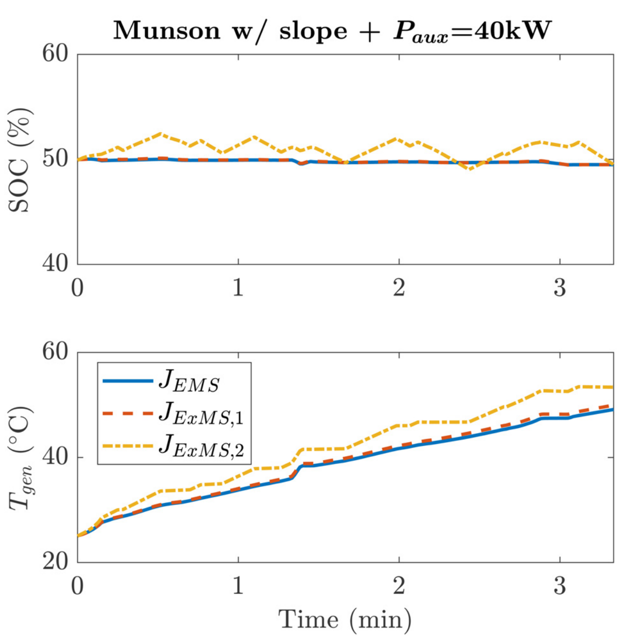

Fig. 22 SOC and generator temperature profiles for J_{EMS}, $J_{\mathrm{ExMS,1}}$, and $J_{\mathrm{ExMS,2}}$ over the Munson with slope mission with auxiliary power

The addition of 40 kW continuous auxiliary power to the Munson driving mission with road slope leads to a higher power request at the wheels, as shown in the first subplot of Fig. 21. Once again, the optimal power-split of $J_{\mathrm{ExMS,2}}$ shows evident differences from the other management strategies. In particular, the thermal emissions ExMS select specific generator powers completely avoiding P_{gen} between 11 kW and 110 kW. Moreover, the battery power P_{batt} drastically changes between intense battery charging around –60 kW and battery discharging around 40 kW, producing a varying SOC profile, illustrated in Fig. 22. Since the optimal P_{gen} is generally higher than Munson with slope without auxiliary power, the generator temperature of every ExMS reaches higher final values as shown in the second subplot of Fig. 22.

The barplot in Fig. 24 summarizes all the results related to FC (Figs. 20 and 23), exergy destruction, and exergy transfer due to heat exchange for all the ExMSs over the different driving missions. The first two subplots of Fig. 24 show that, for every driving mission, the EMS and ExMS for minimization of exergy destruction outperform the thermal emissions strategy in terms of fuel savings and exergy destruction. On the other hand, $J_{\mathrm{ExMS,2}}$ always achieves lower thermal emissions than J_{EMS} and $J_{\mathrm{ExMS,1}}$ over the same driving mission. Therefore, the ExMS for minimization of thermal emissions

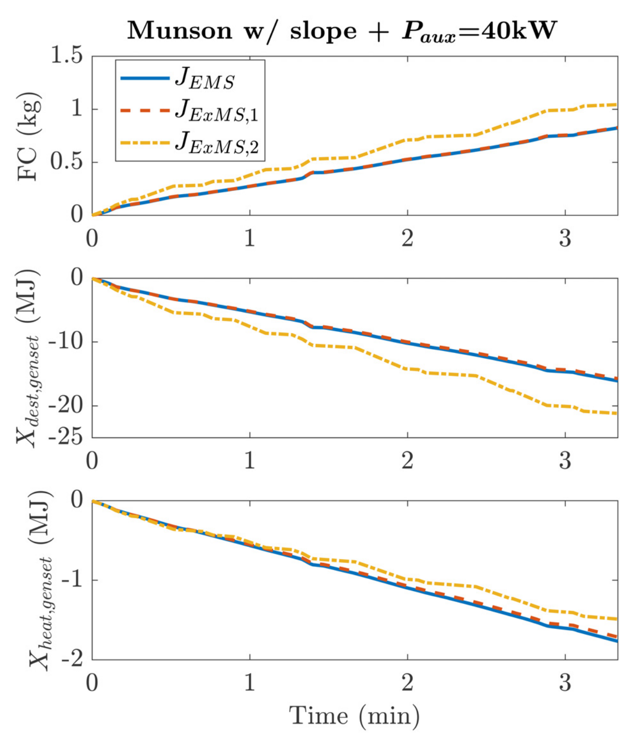

Fig. 23 Cumulative FC, exergy destruction, and exergy related to heat for J_{EMS}, $J_{\mathrm{ExMS,1}}$, and $J_{\mathrm{ExMS,2}}$ over the Munson with slope mission with auxiliary power

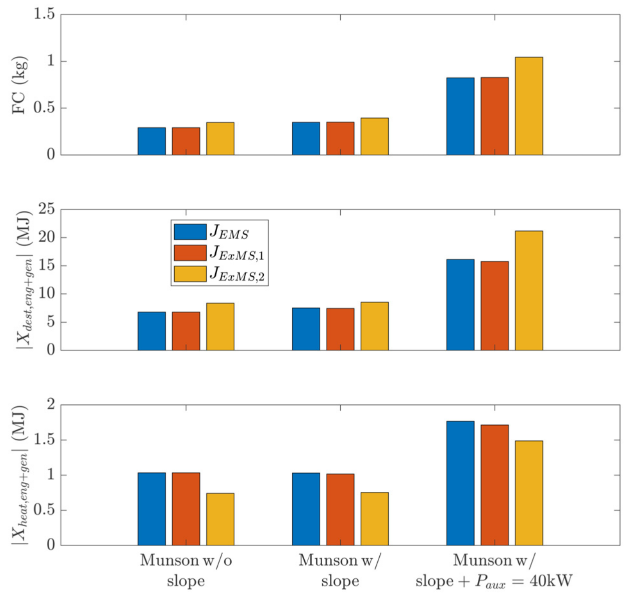

Fig. 24 Cumulative FC, exergy destruction, and exergy related to heat for all the ExMSs over Munson without road slope, and Munson with road slope without and with auxiliary power

Table 3 Computational time

Driving mission	J_{EMS}	$J_{\mathrm{ExMS},1}$	$J_{\mathrm{ExMS},2}$
Munson w/o slope	416 min	412 min	417 min
Munson w/ slope	392 min	391 min	390 min
Munson w/ slope + $P_{\mathrm{aux}} = 40$ kW	382 min	383 min	387 min

proves to be the best strategy to avoid thermal imaging detection. Moreover, the significant increase in FC, $|X_{\mathrm{dest,genset}}|$, and $|X_{\mathrm{heat,genset}}|$ from Munson with slope to Munson with slope + $P_{\mathrm{aux}} = 40$ kW shows the impact of the auxiliary power on the results.

Finally, the computational time required to solve the EMS and ExMSs over all driving missions are shown in Table 3. The experiments were run on a computer with an AMD EPYC 7713 64-Core processor running at 2 GHz, with 512 GB of RAM. The computational times required to solve the EMS and the ExMSs over the same driving mission are very close. Indeed, given the same vehicle model and the same driving mission, the DP computational time is a function of the number, and discretization, of state and control variables [50]. The complexity of the cost function does not influence the computational time required by DP.

5 Conclusions

In this work, novel exergy-based control strategies for ground HEVs are formulated, solved using DP, and compared with the traditional EMS. Starting from the exergetic framework developed in Ref. [22], the energetic and exergetic models of each component of a series military M-ATV HEV are provided. The ICE exergy model, developed in Ref. [24], is adopted and a novel exergy model for IMs is introduced to characterize the exergetic behavior of the electric generator. Afterward, two novel exergy management strategies are formulated as constrained finite-time optimal control problems to minimize specific exergetic terms of the genset system. The first ExMS aims at the minimization of exergy destruction, a quantity representing the irreversibilities of a process, to improve the genset efficiency; the second ExMS minimizes the thermal emissions of the genset to avoid detection in military applications. The solution obtained through DP shows that the first ExMS produces results comparable to those of the standard EMS, achieving at most 0.5% more fuel consumption and 2.5% less exergy destruction than standard EMS. On the other hand, the second ExMS achieves over 19% reduction of thermal emissions, but at least 13% higher fuel consumption and 14% higher exergy destruction than the baseline EMS over the different driving missions. Future works are in the direction of online ExMSs development (such as Adaptive Equivalent Consumption Minimization Strategy [4], Model Predictive Control [51], rule-based strategies [52], etc.) with the solution from the DP serving as a benchmark evaluation strategy.

Acknowledgment

Reference herein to any specific commercial company, product, process, or service by trade name, trademark, manufacturer, or otherwise does not necessarily constitute or imply its endorsement, recommendation, or favoring by the United States Government or the Department of the Army (DoA). The opinions of the authors expressed herein do not necessarily state or reflect those of the United States Government or the DoA, and shall not be used for advertising or product endorsement purposes.

Data Availability Statement

The authors attest that all data for this study are included in the paper.

Nomenclature

A = frontal area (m^2)
c_{fric} = friction coefficient of IM (J)
C = thermal capacity (J/K)
C_r, C_x = roll and drag coefficients
C_1, C_2, C_3 = FMEP coefficients (kPa), (s · kPa), (s^2 · kPa/m^2)
f = volume fraction
f_{IM} = frequency of alternating current of IM (Hz)
F_{brake} = brake mechanical force (N)
FMEP = friction mean effective pressure (Pa)
g = Gibbs free energy (J/mol)
h = specific enthalpy (J/mol)
h_{out} = convective coefficient (W/K)
$\underline{I_1}$ = phasor representation of stator current of IM (A)
$\underline{I_2}$ = phasor representation of rotor current of IM (A)
$\underline{I_C}$ = phasor representation of iron current of IM (A)
I_{cell} = cell current (A)
J = cost function
LHV = fuel lower heating value (J/kg)
M = vehicle mass (kg)
P = Power (W)
$\dot{n}$ = molar flow rate (mol/s)
n_P = number of poles of IM
N_P = number of battery cells connected in parallel
N_S = number of battery cells connected in series
OCV$_{\mathrm{cell}}$ = open circuit voltage of a cell (V)
P_{cyl} = in-cylinder gas pressure (bar)
$P_{\mathrm{fric,IM}}$ = friction power loss of IM (W)
$P_{\mathrm{iron,IM}}$ = iron power loss of IM (W)
$P_{\mathrm{RCL,IM}}$ = rotor copper power loss of IM (W)
$P_{\mathrm{SCL,IM}}$ = stator copper power loss of IM (W)
P_w = power required at the wheels (W)
Q_{cell} = capacity of a cell (Ah)
$Q_{\mathrm{heat,cell}}$ = convective heat exchanged between cell and environment (J)
$R_{0,\mathrm{cell}}$ = internal resistance of a cell (Ω)
R_C = iron resistance of IM (Ω)
R_{gas} = ideal gas constant (J/(mol · K))
R_1 = stator resistance of IM (Ω)
R_2 = rotor resistance of IM (Ω)
s = specific entropy (j/(mol · K))
s_{IM} = slip of IM

S_P = mean piston speed (m/s)
SOC = state of charge of the battery
T = Temperature (K)
T_{cyl} = in-cylinder gas temperature (K)
τ = torque (Nm)
v = vehicle speed (m/s)
$V_{d,\text{tot}}$ = engine displacement (m^3)
$\underline{V_\phi}$ = phasor representation of input phase voltage of IM (V)
x_{EGR} = EGR rate
X = exergy (J)
$X_{\text{comb,eng}}$ = exergy destruction due to combustion irreversibilities (J)
$X_{\text{exh,eng}}$ = exergy transfer of exhaust gas (J)
$X_{\text{fric,eng}}$ = exergy destruction due to friction (J)
$X_{\text{fuel,eng}}$ = exergy related to fuel (J)
$X_{\text{intk,eng}}$ = exergy related to intake air (J)
$X_{\text{others,eng}}$ = exergy destruction of unmodeled phenomena (J)
$X_{\text{work,eng}}$ = exergy related to work (J)
$X1$ = stator reactance of IM (Ω)
$X2$ = rotor reactance of IM (Ω)
x,y = fuel chemical formula coefficients
$\underline{Z_{\text{tot}}}$ = phasor representation of equivalent impedance of the whole IM circuit (Ω)
η = energy efficiency
θ = slope (rad)
λ = air-fuel equivalence ratio
ρ_a = air density (kg/m^3)
$\psi_{\text{ch}},\psi_{\text{ph}}$ = chemical and physical exergy flux J/mol)
ω = rotating speed (rad/s)
ω_{sync} = rotating speed of magnetic field in IM (rad/s)

Notation

batt, cell = subscripts for battery pack and battery cell, respectively
dest, heat = subscripts for exergy destruction and heat exchange
eng, gen, mot = subscripts for internal combustion engine, generator, and motor, respectively
I, E = intake and exhaust gases
IM = subscript for generic Induction Machine
in, out = subscripts for input and output quantities from a system
σ = chemical species
$\underline{\chi}$ = phasor representation of the variable χ: $\underline{\chi} = \chi(\cos\theta_\chi + j\sin\theta_\chi)$, where χ is the amplitude, and θ_χ is the phase angle
$\dot{\chi}$ = time derivative of a variable χ
0 = reference state

Appendix A

In this Appendix, the formulation of the IM power losses as a function of IM speed ω_{IM}, torque τ_{IM}, and temperature T_{IM} is reported. The IM losses terms are derived using the equivalent circuit model of a single phase of the IM, shown in Fig. 25. Each parameter of the equivalent circuit represents a quantity characterizing the stator and rotor windings: R_1 and X_1 are the stator resistance and stator reactance, R_2 and X_2 are the rotor resistance and rotor reactance, X_M is the mutual reactance, and R_C is a fictitious iron resistance. The equivalent circuit parameters values are taken from Ref. [45]. Since the value of the resistance R_C was not provided in Ref. [45], a reasonable value of 100 Ω is assumed[5]. The slip s_{IM} of the IM is an important quantity commonly used to define the relative motion of the rotor and the magnetic field

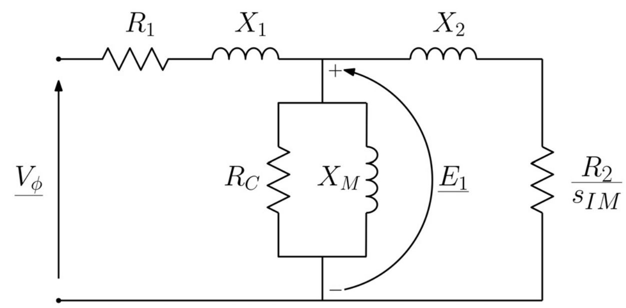

Fig. 25 Equivalent circuit model of an IM

$$s_{\text{IM}} = \frac{\omega_{\text{sync}} - \omega_{\text{IM}}}{\omega_{\text{sync}}} \qquad \omega_{\text{sync}} = \frac{4\cdot\pi\cdot f_{\text{IM}}}{n_P} \tag{A1}$$

where ω_{sync} and ω_{IM} are the rotating speed of the magnetic field and the rotor, respectively, f_{IM} is the frequency of the alternating current and n_P is the number of poles of the machine. The stator and rotor resistances are modeled as a function of the IM temperature T_{IM} [56], i.e., $R_{1/2} = R_{1/2,0}[1 + \alpha\cdot(T_{\text{IM}} - T_0)]$, where $R_{1/2,0}$ is the stator and rotor resistance at the reference temperature T_0 and α is a constant depending on the windings material. The IM is an alternating current electric machine: a phasor representation of currents, voltages, and impedances is required to apply Kirchhoff's laws. Phasor quantities are denoted by an underscore, whereas their amplitude is written without it. Using phasor representation, the following relations hold:

$$\begin{aligned}
\underline{I_1} &= \frac{\underline{V_\phi}}{\underline{Z_{\text{tot}}}} \\
\underline{Z_{\text{tot}}} &= R_1 + jX_1 + \frac{1}{\frac{1}{R_C} + \frac{1}{jX_M} + \frac{1}{R_2/s + jX_2}} \\
\underline{E_1} &= \underline{V_\phi} - (R_1 + jX_1)\cdot\underline{I_1} \\
P_{\text{in,IM}} &= 3\cdot V_\phi\cdot I_1\cdot\cos\theta_{I_1}
\end{aligned} \tag{A2}$$

where $\underline{I_1}$ is the stator current, $\underline{V_\phi}$ is the input voltage, $\underline{Z_{\text{tot}}}$ is the impedance of the entire equivalent circuit, $\underline{E_1}$ is the voltage across the resistance R_C, and θ_{I_1} is the phase angle of the current phasor $\underline{I_1}$. In this study, the Voltage/Frequency Constant Control [57] is used as the low-level IM speed controller. Hence, the following expression is valid for the constant torque region:

$$\frac{V_\phi\cdot\sqrt{3}}{f_{\text{IM}}} = \frac{V_{\text{nom}}}{f_{\text{nom}}} = \text{constant} \tag{A3}$$

where V_{nom} and f_{nom} are the nominal voltage and frequency of the IM. It is now possible to formulate each term of the power losses as a function of the equivalent circuit parameters and currents [36]

$$\begin{aligned}
P_{\text{SCL,IM}} &= 3\cdot R_1\cdot I_1^2 \\
P_{\text{RCL,IM}} &= 3\cdot R_2\cdot I_2^2 \\
P_{\text{iron,IM}} &= 3\cdot\frac{E_1^2}{R_C} \\
P_{\text{out,IM}} + P_{\text{fric,IM}} &= 3\cdot I_2^2\cdot R_2\cdot\left(\frac{1 - s_{\text{IM}}}{s_{\text{IM}}}\right)
\end{aligned} \tag{A4}$$

where I_1 and I_2 are the stator and rotor current. Since the resistances R_1 and R_2 are functions of the temperature T_{IM}, the power losses terms $P_{\text{SCL,IM}}$ and $P_{\text{RCL,IM}}$ are directly influenced by T_{IM}; hence, η_{IM}

[5]In Refs. [53,54], and [55], the iron resistance for different IMs ranges between 10 Ω and 10^4 Ω

is also a function of T_{IM}. The friction losses are proportional to the speed ω_{IM}, through the friction coefficient c_{fric} [46], i.e., $P_{fric,IM} = c_{fric} \cdot \omega_{IM}$. $P_{out,IM}$ is obtained using the following equation: $P_{out,IM} = \omega_{IM} \cdot \tau_{IM}$. While $P_{out,IM}$ and $P_{fric,IM}$ are directly calculated from ω_{IM} and τ_{IM}, the system of Eqs. (8), (A1)–(A4) is solved to calculate the other power losses terms $P_{SCL,IM}$, $P_{RCL,IM}$, and $P_{iron,IM}$ for every triplet (ω_{IM}, τ_{IM}, T_{IM}). The MATLAB function `fsolve` with the trust-region-dogleg algorithm [58] is adopted to solve the system of equations.

Appendix B

For the sake of completeness, we explain how the optimal operating line for the minimization of the genset exergy destruction $|\dot{X}_{dest,genset}|$ is obtained. The same approach can be used to obtain the OOLs for EMS and ExMS for minimization of thermal emissions. The optimal operating line is defined as the set of operating points (ω_{eng}, τ_{eng}) owing to the lowest $|\dot{X}_{dest,genset}|$ of those on constant-power curves [59]. Every ICE power request P_{eng} can be delivered by the set of operating points that satisfy the equation

$$P_{eng} = \omega_{eng} \cdot \tau_{eng} \tag{B1}$$

For a generic P_{eng} value, the optimal operating point is the one that minimizes the quantity $|\dot{X}_{dest,genset}|$ between the set of operating points which satisfy Eq. (B1). The optimal operating line is determined by selecting the optimal operating point for each value of a discretized set of the engine power P_{eng}.

Appendix C

For a given ICE power, the in-cylinder gas to wall heat transfer increases with torque due mainly to the increasing in-cylinder gas temperature [41]. This phenomenon can be explained by analyzing the ICE T_{cyl} map and computing the relative minimum gas temperature line from the ICE model [24]. Indeed, the minimum in-cylinder gas temperature line, which is defined as the set of operating points that have the lowest T_{cyl} of those on constant-power curves, is located at high-speed regions, as shown in Fig. 26. Therefore, the ExMS for the minimization of thermal emissions tends to select high-speed operating points to obtain lower T_{cyl}, with a consequently lower exergy transfer due to the heat exchange between the ICE and the environment.

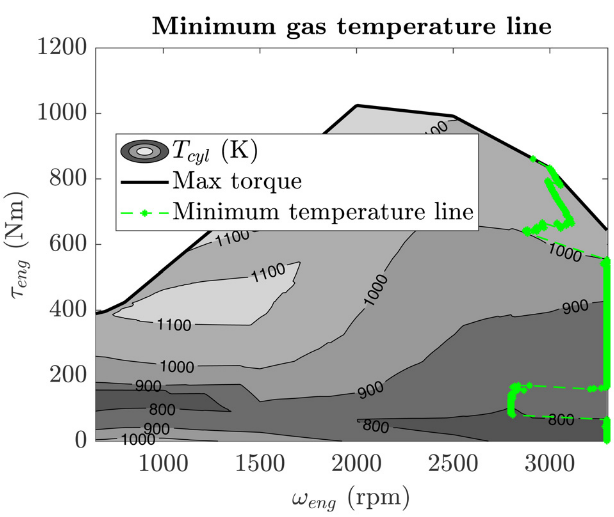

Fig. 26 In-cylinder gas temperature map and minimum temperature line

References

[1] Mittal, V., Novoselich, B., and Rodriguez, A., 2022, "Hybridization of us Army Combat Vehicles," SAE Paper No. 2022-01-0371.

[2] Wahlman, A., 2014, "The M1 Abrams," Mil. Rev., pp. 11–20.

[3] Kramer, D. M., and Parker, G. G., 2011, "Current State of Military Hybrid Vehicle Development," Int. J. Electric Hybrid Veh., **3**(4), pp. 369–387.

[4] Onori, S., Serrao, L., and Rizzoni, G., 2016, *Hybrid Electric Vehicles: Energy Management Strategies*, Springer, Berlin.

[5] Moorhouse, D. J., and Camberos, J. A., 2011, *Exergy Analysis and Design Optimization for Aerospace Vehicles and Systems*, American Institute of Aeronautics and Astronautics, Reston, VA.

[6] Tsatsaronis, G., 2007, "Definitions and Nomenclature in Exergy Analysis and Exergoeconomics," Energy, **32**(4), pp. 249–253.

[7] Ebrahimgol, H., Aghaie, M., Zolfaghari, A., and Naserbegi, A., 2020, "A Novel Approach in Exergy Optimization of a wwer1000 Nuclear Power Plant Using Whale Optimization Algorithm," Ann. Nucl. Energy, **145**, p. 107540.

[8] Kallio, S., and Siroux, M., 2020, "Energy Analysis and Exergy Optimization of Photovoltaic-Thermal Collector," Energies, **13**(19), p. 5106.

[9] Dong, Z., Li, D., Wang, Z., and Sun, M., 2018, "A Review on Exergy Analysis of Aerospace Power Systems," Acta Astronaut., **152**, pp. 486–495.

[10] Hayes, D., Lone, M., Whidborne, J. F., Camberos, J., and Coetzee, E., 2017, "Adopting Exergy Analysis for Use in Aerospace," Prog. Aerosp. Sci., **93**, pp. 73–94.

[11] Naserbegi, A., and Aghaie, M., 2021, "Exergy Optimization of Nuclear-Solar Dual Proposed Power Plant Based on GWO Algorithm," Prog. Nucl. Energy, **140**, p. 103925.

[12] James, C., Kim, T. Y., and Jane, R., 2020, "A Review of Exergy Based Optimization and Control," Processes, **8**(3), p. 364.

[13] Razmara, M., Maasoumy, M., Shahbakhti, M., and Robinett, R. III, 2015, "Optimal Exergy Control of Building HVAC System," Appl. Energy, **156**, pp. 555–565.

[14] Jain, N., and Alleyne, A., 2015, "Energy-Based Optimal Control of a Vapor Compression System," Energy Convers. Manage., **92**, pp. 353–365.

[15] Ray, T. K., Ganguly, R., and Gupta, A., 2013, "Optimal Control Strategy for Minimization of Exergy Destruction in Boiler Superheater," Energy Convers. Manage., **66**, pp. 234–245.

[16] Trinklein, E. H., Parker, G. G., McCoy, T. J., Robinett, R. D., and Weaver, W. W., 2018, "Reduced Order Multi-Domain Modeling of Shipboard Systems for Exergy-Based Control Investigations," Nav. Eng. J., **130**(3), pp. 87–105.

[17] Trinklein, E. H., Parker, G. G., and McCoy, T. J., 2020, "Modeling, Optimization, and Control of Ship Energy Systems Using Exergy Methods," Energy, **191**, p. 116542.

[18] Rakopoulos, C. D., and Giakoumis, E. G., 2006, "Second-Law Analyses Applied to Internal Combustion Engines Operation," Prog. Energy Combust. Sci., **32**(1), pp. 2–47.

[19] Canakci, M., and Hosoz, M., 2006, "Energy and Exergy Analyses of a Diesel Engine Fuelled With Various Biodiesels," Energy Sources, Part B, **1**(4), pp. 379–394.

[20] Sayin Kul, B., and Kahraman, A., 2016, "Energy and Exergy Analyses of a Diesel Engine Fuelled With Biodiesel-Diesel Blends Containing 5% Bioethanol," Entropy, **18**(11), p. 387.

[21] Razmara, M., Bidarvatan, M., Shahbakhti, M., and Robinett, R.D, III. 2016, "Optimal Exergy-Based Control of Internal Combustion Engines," Appl. Energy, **183**, pp. 1389–1403.

[22] Dettù, F., Pozzato, G., Rizzo, D. M., and Onori, S., 2021, "Exergy-Based Modeling Framework for Hybrid and Electric Ground Vehicles," Appl. Energy, **300**, p. 117320.

[23] Brzezanski, M., and Mezyk, P., 2017, "Heat Balance of the Military Vehicle," Combust. Engines, **56**(3), pp. 131–134.

[24] Pozzato, G., Rizzo, D. M., and Onori, S., 2022, "Mean-Value Exergy Modeling of Internal Combustion Engines: Characterization of Feasible Operating Regions," ASME J. Dyn. Syst. Meas. Contr., **144**(6), p. 061009.

[25] Pozzato, G., Rizzo, D., and Onori, S., 2022, "Sensitivity Analysis of a Mean-Value Exergy-Based Internal Combustion Engine Model," SAE Paper No. 2022-01-0356.

[26] Mamun, A.-A., Liu, Z., Rizzo, D. M., and Onori, S., 2019, "An Integrated Design and Control Optimization Framework for Hybrid Military Vehicle Using Lithium-Ion Battery and Supercapacitor as Energy Storage Devices," IEEE Trans. Transp. Electrif., **5**(1), pp. 239–251.

[27] Kim, Y., Salvi, A., Siegel, J. B., Filipi, Z. S., Stefanopoulou, A. G., and Ersal, T., 2014, "Hardware-in-the-Loop Validation of a Power Management Strategy for Hybrid Powertrains," Control Eng. Pract., **29**, pp. 277–286.

[28] Mi, C., and Masrur, M. A., 2017, *Hybrid Electric Vehicles: Principles and Applications With Practical Perspectives*, Wiley, Hoboken, NJ.

[29] Serrao, L., Onori, S., and Rizzoni, G., 2011, "A Comparative Analysis of Energy Management Strategies for Hybrid Electric Vehicles," ASME J. Dyn. Syst. Meas. Contr., **133**(3), p. 031012.

[30] Rosen, M. A., 2004, "Exergy Analysis of Waste Emissions," *Encyclopedia of Energy*, C. J. Cleveland, ed., Elsevier, New York, pp. 623–632.

[31] Catenaro, E., Rizzo, D. M., and Onori, S., 2021, "Experimental Analysis and Analytical Modeling of Enhanced-Ragone Plot," Appl. Energy, **291**, p. 116473.

[32] Catenaro, E., and Onori, S., 2021, "Experimental Data of Lithium-Ion Batteries Under Galvanostatic Discharge Tests at Different Rates and Temperatures of Operation," Data Brief, **35**, p. 106894.

[33] Allam, A., Onori, S., Marelli, S., and Taborelli, C., 2015, "Battery Health Management System for Automotive Applications: A Retroactivity-Based Aging

Propagation Study," 2015 American Control Conference (ACC), IEEE, Chicago, IL, July 1–3, pp. 703–716.
[34] Tanim, T. R., Shirk, M. G., Bewley, R. L., Dufek, E. J., and Liaw, B. Y., 2018, "Fast Charge Implications: Pack and Cell Analysis and Comparison," J. Power Sources, **381**, pp. 56–65.
[35] Bohacek, J., Raudensky, M., and Karimi-Sibaki, E., 2019, "Polymeric Hollow Fibers: Uniform Temperature of li-Ion Cells in Battery Modules," Appl. Therm. Eng., **159**, p. 113940.
[36] Chapman, S., 2005, *Electric Machinery Fundamentals*, The McGraw-Hill Companies, New York.
[37] Goundar, S., Pillai, M., Mamun, K., Islam, F., and Deo, R., 2015, "Real Time Condition Monitoring System for Industrial Motors," 2015 2nd Asia-Pacific World Congress on Computer Science and Engineering (APWC on CSE), IEEE, Nadi, Fiji, Dec. 2–4, pp. 1–9.
[38] Bellman, R., 2003, *Dynamic Programming*, Dover Publications, Mineola, NY.
[39] Böhme, T. J., and Frank, B., 2017, *Hybrid Systems, Optimal Control and Hybrid Vehicles*, Springer International, Cham, Switzerland, pp. 401–428.
[40] Sundstrom, O., and Guzzella, L., 2009, "A Generic Dynamic Programming Matlab Function," 2009 IEEE Control Applications, (CCA) & Intelligent Control, (ISIC), IEEE, St. Petersburg, Russia, July 8–10, pp. 1625–1630.
[41] Caton, J. A., 2000, "Operating Characteristics of a Spark-Ignition Engine Using the Second Law of Thermodynamics: Effects of Speed and Load," SAE Paper No. 2000-01-0952.
[42] Koprubasi, K., 2008, "Modeling and Control of a Hybrid-Electric Vehicle for Drivability and Fuel Economy Improvements," Ph.D. thesis, The Ohio State University, Columbus, OH.
[43] Arata, J., Leamy, M., and Cunefare, K., 2012, "Power-Split Hev Control Strategy Development With Refined Engine Transients," SAE Int. J. Altern. Powertrains, **1**(1), pp. 119–133.
[44] Liu, Z., Mamun, A.-A. M., Rizzo, D. M., and Onori, S., 2018, "Combined Battery Design Optimization and Energy Management of a Series Hybrid Military Truck," SAE Int. J. Altern. Powertrains, **7**(2), pp. 155–168.
[45] Riaz, M., 2011, "Simulation of Electric Machine and Drive Systems," accessed Oct. 23, 2023, http://people.ece.umn.edu/users/riaz/
[46] MATLAB, 2022, "Asynchronous Machine," accessed Oct. 23, 2023, https://www.mathworks.com/help/sps/powersys/ref/asynchronousmachine.html
[47] Miegeville, L., Guerin, P., and Dreulle, D., 2014, "Investigation of Correlations Between Driving Patterns and Power Demand of Auxiliary Devices aboard Military Vehicles," 2014 IEEE Vehicle Power and Propulsion Conference (VPPC), IEEE, Coimbra, Portugal, Oct. 27–30, pp. 1–6.
[48] Rousseau, G., Sinoquet, D., and Rouchon, P., 2007, "Constrained Optimization of Energy Management for a Mild-Hybrid Vehicle," Oil Gas Sci. Technol.-Rev. l'IFP, **62**(4), pp. 623–634.
[49] Butt, J. R., 2005, "A Study of Morphing Wing Effectiveness in Fighter Aircraft Using Exergy Analysis and Global Optimization Techniques," Ph.D. thesis, Virginia Tech, Blacksburg, VA.
[50] De Madrid, A., Dormido, S., and Mozrilla, F., 1999, "Reduction of the Dimensionality of Dynamic Programming: A Case Study," Proceedings of the 1999 American Control Conference, IEEE, San Diego, CA, June 2–4, Vol. 4, pp. 2852–2856.
[51] Sampathnarayanan, B., Serrao, L., Onori, S., Rizzoni, G., and Yurkovich, S., 2009, "Model Predictive Control as an Energy Management Strategy for Series Hybrid Electric Vehicles," ASME Paper No. GTP-19-1460.
[52] Grizzle, J. W., Lin, C. C., Peng, H., and Kang, J. M., 2003, "Power Management Strategy for a Parallel Hybrid Electric Truck," IEEE Trans. Control Syst. Technol., **11**(6), pp. 839–849.
[53] Bazzi, A. M., and Krein, P. T., 2010, "Review of Methods for Real-Time Loss Minimization in Induction Machines," IEEE Trans. Ind. Appl., **46**(6), pp. 2319–2328.
[54] Torrent, M., and Blanqué, B., 2021, "Influence of Equivalent Circuit Resistances on Operating Parameters on Three-Phase Induction Motors With Powers Up to 50 kw," Energies, **14**(21), p. 7130.
[55] Nasir, B. A., 2020, "An Accurate Iron Core Loss Model in Equivalent Circuit of Induction Machines," J. Energy, **2020**, pp. 1–10.
[56] Wu, Y., and Gao, H., 2006, "Induction-Motor Stator and Rotor Winding Temperature Estimation Using Signal Injection Method," IEEE Trans. Ind. Appl., **42**(4), pp. 1038–1044.
[57] Blaabjerg, F., 2018, *Control of Power Electronic Converters and Systems: Volume 2*, Vol. 2, Academic Press, New York.
[58] Nocedal, J., and Wright, S. J., 1999, *Numerical Optimization*, Springer, New York.
[59] Ahn, K., and Papalambros, P., 2009, "Engine Optimal Operation Lines for Power-Split Hybrid Electric Vehicles," Proc. Inst. Mech. Eng., Part D, **223**(9), pp. 1149–1162.